CHALMERS
UNIVERSITY OF TECHNOLOGY

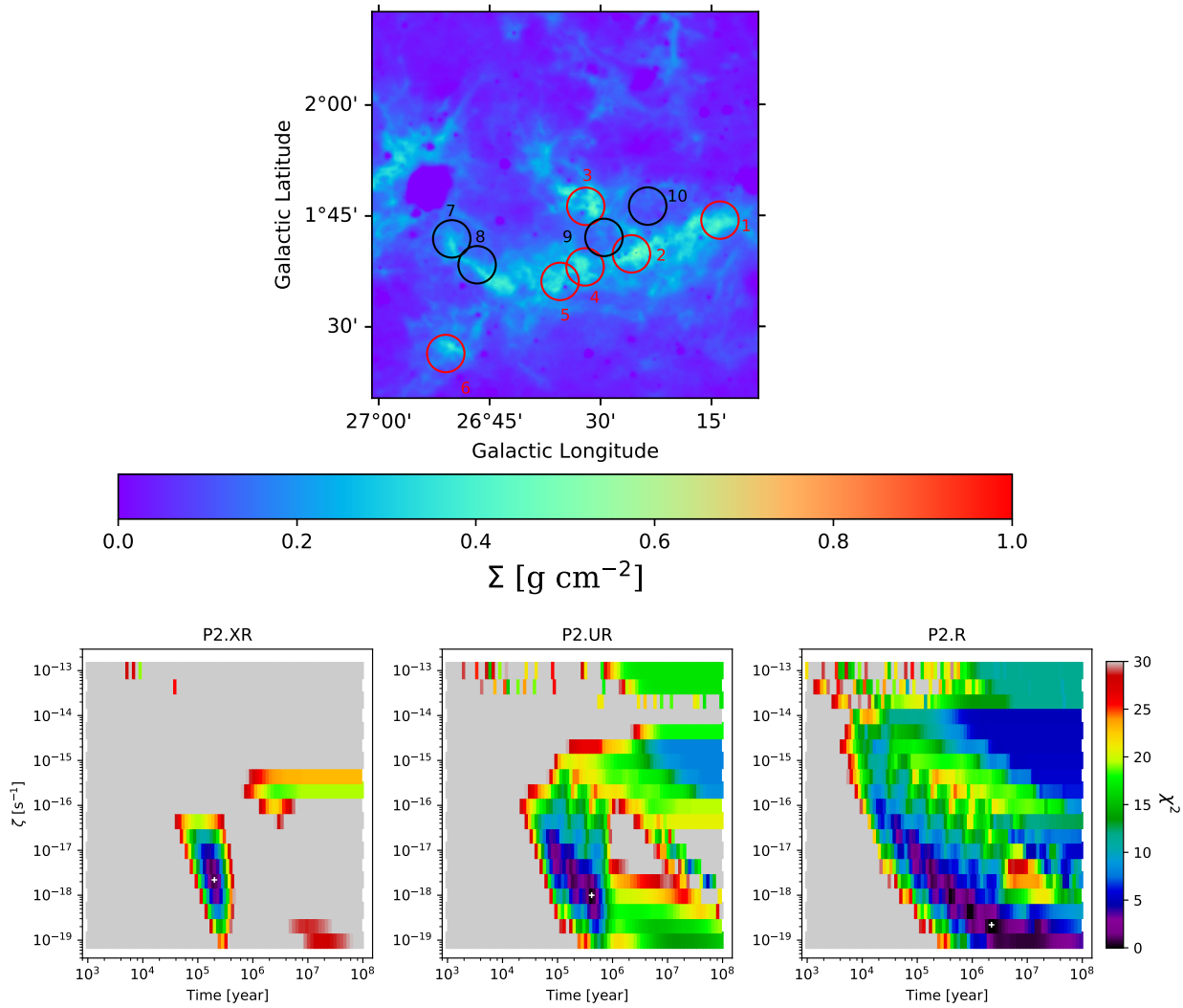

Astrochemical Modeling of Infrared Dark Clouds

NEGAR ENTEKHABI

Department of Physics
CHALMERS UNIVERSITY OF TECHNOLOGY
Gothenburg, Sweden 2021

Master's thesis 2021

Astrochemical Modeling of Infrared Dark Clouds

NEGAR ENTEKHABI

CHALMERS
UNIVERSITY OF TECHNOLOGY

Department of Physics
Department of Space,Earth and Environment
Chalmers University of Technology
Gothenburg, Sweden 2021

Astrochemical Modeling of Infrared Dark Clouds

© NEGAR ENTEKHABI, 2021.

Supervisors: Prof.Jonathan C. Tan
Examiner: Prof.Jonathan C. Tan

Master's Thesis 2021
Department of Physics
Chalmers University of Technology
SE-412 96 Gothenburg
Telephone +46 31 772 1000

Cover: *Top*: MIREX derived mass surface density map of IRDC G28.37+00.07 from (scalebar is in $\mathrm{g\,cm^{-2}}$).*Bottom*: The projected best χ^2 values in the ζ versus t plane for the P2 position in the cloud, for the XR (left), UR (middle) and R (right) search methods with Case 1 (fitting to abundances of CO, HCO^+ and N_2H^+).

Typeset in LaTeX
Gothenburg, Sweden 2021

Abstract

Infrared Dark Clouds (IRDCs) are cold, dense regions of the interstellar medium (ISM) that are likely to represent the initial conditions for massive star and star cluster formation. It is thus important to study the physical and chemical conditions of IRDCs to provide constraints and inputs for theoretical models of these processes. We aim to determine the astrochemical conditions, especially cosmic ray ionization rate (CRIR) and chemical age, in different regions of the massive IRDC G28.37+00.07 by comparing observed abundances of multiple molecules and molecular ions with the predictions of astrochemical models. We have computed a series of single-zone, time-dependent, astrochemical models with a gas-grain network that systematically explores the parameter space of density, temperature, CRIR, and visual extinction. We have also investigated the effects of choices of CO ice binding energy and temperatures achieved in transient heating of grains when struck by cosmic rays. We selected 10 positions across the IRDC that are known to have a variety of star formation activity. We utilised mid-infrared (MIR) extinction maps and sub-mm emission maps to measure the mass surface densities of these regions, needed for abundance and volume density estimates. The sub-mm emission maps were also used to measure temperatures. We then used IRAM-30m observations of various tracers, especially $C^{18}O$(1-0), $H^{13}CO^+$(1-0), $HC^{18}O^+$(1-0), and N_2H^+(1-0), to estimate column densities and thus abundances. Finally, we investigated the range of astrochemical conditions that are consistent with the observed abundances.

Results: The typical physical conditions of the IRDC regions are $n_{\rm H} \sim 3 \times 10^4$ to 10^5 cm^{-3} and $T \simeq 10$ to 15 K. Strong emission of $H^{13}CO^+$(1-0) and N_2H^+(1-0) is detected towards all the positions and these species are used to define relatively narrow velocity ranges of the IRDC regions, which are used for estimates of CO abundances, via $C^{18}O$(1-0). CO depletion factors are estimated to be in the range $f_D \sim 3$ to 10. Using estimates of the abundances of CO, HCO^+ and N_2H^+ we find consistency with astrochemical models that have relatively low CRIRs of $\zeta \sim 10^{-18}$ to $\sim 10^{-17}$ s^{-1}, with no evidence for systematic variation with the level of star formation activity. Astrochemical ages, defined with reference to an initial condition of all H in H_2, all C in CO, and all other species in atomic form, are found to be < 1 Myr. We also explore the effects of using other detected species, i.e., HCN, HNC, HNCO, CH_3OH, and H_2CO, to constrain the models. These generally lead to implied conditions with higher levels of CRIRs and older chemical ages. Considering the observed f_D versus $n_{\rm H}$ relation of the 10 positions, which we find to have relatively little scatter, we discuss potential ways in which the astrochemical models can match such a relation as a quasi-equilibrium limit valid at ages of at least a few free-fall times, i.e., $\gtrsim 0.3$ Myr, including the effect of CO envelope contamination, small variations in temperature history near 15 K, CO-ice binding energy uncertainties and CR induced desorption. We find general consistency with the data of ~ 0.5 Myr-old models that have $\zeta \sim 2 - 5 \times 10^{-18}$ s^{-1} and CO abundances set by a

balance of freeze-out with CR induced desorption.

Conclusions: We have constrained the astrochemical conditions in 10 regions in a massive IRDC, finding evidence for relatively low values of CRIR compared to diffuse ISM levels. We have not seen clear evidence for variation in the CRIR with the level of star formation activity. We favour models that involve relatively low CRIRs ($\lesssim 10^{-17}\,\mathrm{s}^{-1}$) and relatively old chemical ages ($\gtrsim 0.3\,\mathrm{Myr}$, i.e., $\gtrsim 3t_{\mathrm{ff}}$). We discuss potential sources of systematic uncertainties in these results and the overall implications for IRDC evolutionary history and astrochemical models.

Keywords. astrochemistry – molecular clouds – star formation

Contents

List of Figures

List of Tables

1

Introduction

Infrared Dark Clouds (IRDCs) are cold ($T < 25\,\mathrm{K}$) (e.g., Pillai et al., 2006; Peretto et al., 2010; Lim et al., 2016) and dense ($n_\mathrm{H} \gtrsim 10^3\ \mathrm{cm}^{-3}$) (e.g., Kainulainen and Tan, 2013; Lim et al., 2016) regions of the interstellar medium (ISM) that have the potential to host the formation of massive stars and star clusters (for a review, see, e.g., Tan et al., 2014). Thus, it is important to study the physical and chemical properties of IRDCs to understand the initial conditions for the formation of these massive stellar systems.

One important astrochemical process that is expected to occur in the cold, dense conditions of IRDCs is the freeze-out of certain molecules to form ice mantles around dust grains, thus depleting their abundance in the gas phase. The CO depletion factor ($f_\mathrm{D,CO}$), is defined as the ratio of the CO gas phase abundance if all C was present as gas phase CO compared to the actual abundance. For example, in the filamentary IRDC G035.39-00.33 (Cloud H) this depletion factor has been measured to be ~ 3 on parsec scales by Hernandez et al. (2012) and up to ~ 10 in some positions by Jiménez-Serra et al. (2014).

High CO depletion factors are generally expected in cold conditions, i.e., when $T \lesssim 20\,\mathrm{K}$. The rate of CO depletion scales inversely with density and the timescale to achieve a high depletion factor can be relatively short, i.e., shorter than the free-fall time for densities $n_\mathrm{H} \gtrsim 10^3\ \mathrm{cm}^{-3}$. In this cold temperature regime, the equilibrium abundance of gas phase CO is then expected to be set by a balance between the freeze-out rate and rates of non-thermal desorption processes, e.g., photo-desorption (including by UV photons induced by cosmic rays [CRs]) and by direct CR desorption, e.g., due to localized transitory heating of dust grains when impacted by a CR (Hasegawa and Herbst, 1993). While CO and other species, such as H_2O, are expected to be heavily depleted in cold, dense conditions, from studies of low-mass cores it has been inferred that N-bearing species suffer lower amounts of depletion (e.g., Caselli et al., 1999; Crapsi et al., 2007).

In regions where CO is highly depleted and the ortho-to-para ratio of H_2 has declined to small values, another astrochemical process that is expected to occur is the build up relatively large abundances of H_2D^+, which in turn can lead to the deuteration of species such N_2H^+. Relatively high levels of deuteration of N_2H^+ have been observed in IRDCs on both parsec scales (Barnes et al., 2016) and in more localised, sub-parsec scale cores (e.g., Kong et al., 2016). These studies have concluded that the conditions in these IRDCs are likely to be relatively chemically evolved, i.e., with the gas having been in a cold and dense state for at least several local free-fall times, in order to achieve the high levels of deuteration that are observed. However, this is not a unique solution: models of relatively rapid collapse of cores can achieve

the high observed levels of deuteration if the CR ionization rate (CRIR) is relatively high. For example, Hsu et al. (2021) have presented models of a massive (60 $M_\odot$) core that can achieve abundance ratios of $[N_2D^+]$ / $[N_2H^+] \sim 0.1$ within one free-fall time of $\sim 80,000$ yr if the CRIR is $\sim 10^{-16}$ s^{-1}.

In addition to the deuteration process, much of interstellar chemistry is driven by CR ionization, and the CRIR, ζ, (defined as the rate of ionizations per H nucleus) is an important parameter of astrochemical models. Examples of inferred values of CRIR include the study of the $H^{13}CO^+$ emission and H_3^+ absorption towards seven massive protostellar cores by van der Tak and van Dishoeck (2000), who estimated $\zeta \sim (2.6 \pm 1.8) \times 10^{-17}$ s^{-1}. More recent studies of hot cores with more sophisticated chemical networks include the work of Barger and Garrod (2020), who derived more elevated levels of CRIRs.

Studies of the diffuse ISM have found values of $\zeta \simeq 2 \times 10^{-16}$ s^{-1} (e.g., Neufeld and Wolfire, 2017). In regions of active star formation, such as OMC-2 FIR 4, much higher values of CRIR, $\gtrsim 10^{-15}$ s^{-1}, have been reported (Ceccarelli et al., 2014a; Fontani et al., 2017; Favre et al., 2018), which may be explained by local production in protostellar accretion and/or outflow shocks (Padovani et al., 2016; Gaches and Offner, 2018). Another region where the CRIR is inferred to be very high is the Galactic Centre, with values of $\zeta \gtrsim 10^{-15}$ s^{-1} (Carlson et al., 2016).

Lower energy CRs, which dominate the CRIR, are expected to be absorbed by high column densities of gas and more easily shielded by magnetic fields, whose strength increases in denser regions (Crutcher, 2012). Thus, it is possible that the CRIR in IRDCs may be smaller than that of the diffuse ISM in which they reside. To date, there have been relatively few studies of the CRIR in IRDCs.

IRDCs have the advantage of being probed by mid-infrared (MIR) extinction (MIREX) mapping methods (e.g., Butler and Tan, 2009,0; Kainulainen and Tan, 2013), which yield measurements of cloud mass surface density, Σ. *Herschel* sub-mm emission maps also constrain Σ and additionally provide a measure of the dust temperature, although careful subtraction of contributions from the diffuse Galactic plane are important (Lim et al., 2016). IRDCs are expected to be at a relatively early evolutionary stage, which should simplify their modeling, especially with respect to hot cores (e.g., van der Tak and van Dishoeck, 2000; Gieser et al., 2019). However, studies with ALMA and *Herschel* do indicate that active star formation can be proceeding even in MIR-dark regions of the clouds (e.g., Tan et al., 2016; Kong et al., 2019; Moser et al., 2020).

In this paper, we aim to constrain the astrochemical conditions, including CRIR and chemical age, in ten different positions in the massive IRDC G28.37+00.07. We first present a grids of astrochemical models, based on the work of Walsh et al. (2015), that cover a wide range of physical conditions, including those relevant to IRDCs (§2). We next, in §3, measure the physical properties of mass surface density (Σ), number density (n_H) and temperature (T) of the IRDC regions, followed by measurements of the column densities and thus abundances of various molecules and molecular ions from IRAM-30m telescope observations. Then, in §4, we first discuss the derived abundances, then determine which parts of the multi-dimensional astrochemical model parameter space, including CRIR and time, are consistent with the observations. We also discuss potential effects of systematic uncertainties in the

measurements of abundances and astrochemical modeling. We present our conclusions in §6.

2

Astrochemical Model

2.1 Overview of the Model

We use the astrochemical model developed by Walsh et al. (2015) to predict the evolution of abundances of different species in the gas and grain ice mantle phases. The model uses a gas-phase network extracted from the UMIST 2012 Database for Astrochemistry (McElroy et al., 2013), complemented by both thermal and non-thermal gas-grain processes, including CR-induced thermal desorption (CRID) (with standard value for CR-induced temperature of $T_{\rm CRID} = 70$ K), photodesorption, X-ray desorption, and grain-surface reactions. The reaction types included in the astrochemical code are described in Walsh et al. (2010) and the subsequent works (Walsh et al., 2012,0; Walsh et al., 2014,0).

For the first model grid ("Grid 1") we have adopted the default CO ice binding energy of 855 K and we have switched off CR-induced thermal desorption reactions (Hasegawa and Herbst, 1993), since their rates are highly uncertain (Cuppen et al., 2017). Still, CR-induced photoreactions are included, including those that lead to desorption of species from grain surfaces. Grid 1 is the fiducial model we have used for most of our investigation. However, as we discuss later, after comparison with the observational results we find the need to investigate the following changes in the astrochemical modeling, i.e., "Grid 2": an increase in the CO ice binding energy to 1100 K, relevant in more realistic situations in which CO is mixed with water ice (Öberg et al., 2005; Cuppen et al., 2017); CRID reactions turned on with various values of $T_{\rm CRID}$ explored up to about 100 K. In all of our modeling we do not include any X-ray background, so the reactions involving X-rays do not play any role.

Overall the network includes a total of 8763 reactions following the time evolution of the abundances of 669 species. The elements that are followed in the network and their assumed initial abundances are shown in Table 2.1. All elements are initially in atomic form, except for: H, which is almost entirely in the form of H_2; C, which is entirely in the form of CO; and 44% of O that is in the form of CO. This choice is made given that IRDCs are expected to typically be structures within larger-scale molecular clouds.

Table 2.1: Fiducial Initial Abundances

Species	Abundance (n_X/n_H)
H_2	5.00e-01
H	5.00e-05
He	9.75e-02
CO	1.40e-04
O	1.80e-04
N	7.50e-05
S	8.00e-08
F	2.00e-08
Si	8.00e-09
Cl	4.00e-09
P	3.00e-09
GRAIN	1.30e-12

We have adopted the standard parameter values of a Draine FUV radiation field equal to 6.4×10^{-3} erg cm^{-2} s^{-1} and a Habing FUV field equal to 4.0×10^{8} cm^{-2} s^{-1}. Other standard parameters are the assumed dust particle radius of $a_0 = 0.1$ μm, so that the grain surface area per H nucleus is 1.63×10^{-19} cm^2.
Each astrochemical model in a grid is run for a fixed set of values of number density of H nuclei (n_H), gas temperature (T), CRIR (ζ), visual extinction (A_V), and FUV radiation field intensity (G_0). The range of the parameter space of the grid of the models for this work is presented in Table 2.2. This parameter space is sampled at a resolution of 3 values per decade for density and CRIR. For temperatures, with a focus on lower values, we run models at 5, 10, 15, 20, 25, 30, 40, 50, ..., 100, 120, ..., 200, 250, 300, ..., 500, 600, ..., 1000 K. For A_V, we run models at 1, 2, 3, 4, 5, 7, 10, 20, 50, 100 mag.
We only run models with one value of external FUV radiation field, i.e., $G_0 = 4$, which is the value expected in the inner Galaxy relevant to most IRDCs (Wolfire et al., 2010). In any case, the typical values of extinctions in IRDCs are very high, so that the external FUV radiation field is expected to play a negligible role in the chemical evolution.
With the above choices, we have a total of 137,750 different physical models in each grid. Each of these models is evolved in time for 10^8 years, with a sampling of 100 outputs per decade in time (after 10^3 years). We note that while we have developed here a relatively wide range of models for a first general exploration, when modeling IRDCs, we will focus on a much narrower range of conditions that are constrained by observational data on the clouds.

Table 2.2: Model Grid Parameter Space

Parameter	Explored Range
$n_{\rm H}$ (cm^{-3})	10 - 10^9
T (K)	5 - 1000
ζ (s^{-1})	10^{-19} - 10^{-13}
A_V (mag)	1 - 100
G_0 (Habings)	4

2.2 CO Depletion Factor

In this section we study how the CO depletion factor, f_D, varies with astrochemical conditions. CO is typically the second most abundant molecule in molecular clouds after H_2 and so it is important to understand its behaviour. One of the main expectations is that CO freezes out rapidly from the gas phase at temperatures $\lesssim$ 20 K, but then with eventual abundances set by a balance of the non-thermal desorption processes from the grains.

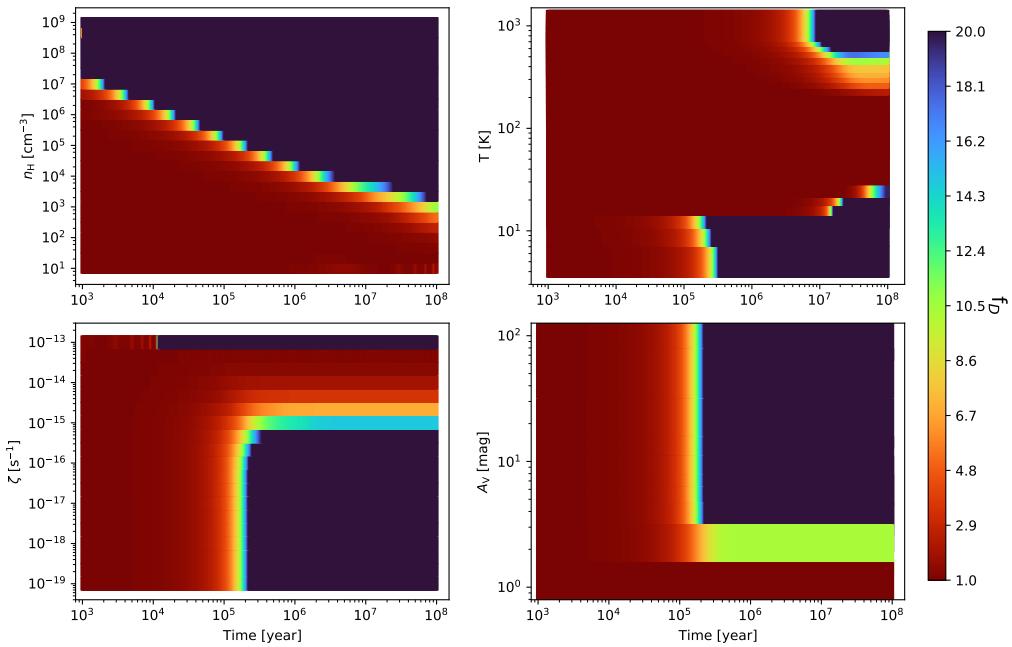

Figure 2.1: Time evolution of CO depletion factor, f_D, evaluated in astrochemical model Grid 1 as a function of the environmental variables of: (a) top left - number density of H nuclei, $n_{\rm H}$; (b) top right - temperature, T; (c) bottom left - cosmic ray ionization rate, ζ; (d) bottom right - visual extinction, A_V. In each panel the three remaining variables are held fixed at their fiducial level, i.e., $n_{\rm H} = 10^5$ cm^{-3}, $T = 15$ K, $\zeta = 10^{-17}$ s^{-1}, $A_V = 100$ mag. Each time-evolving model is shown by a horizontal line with f_D indicated by the color scale.

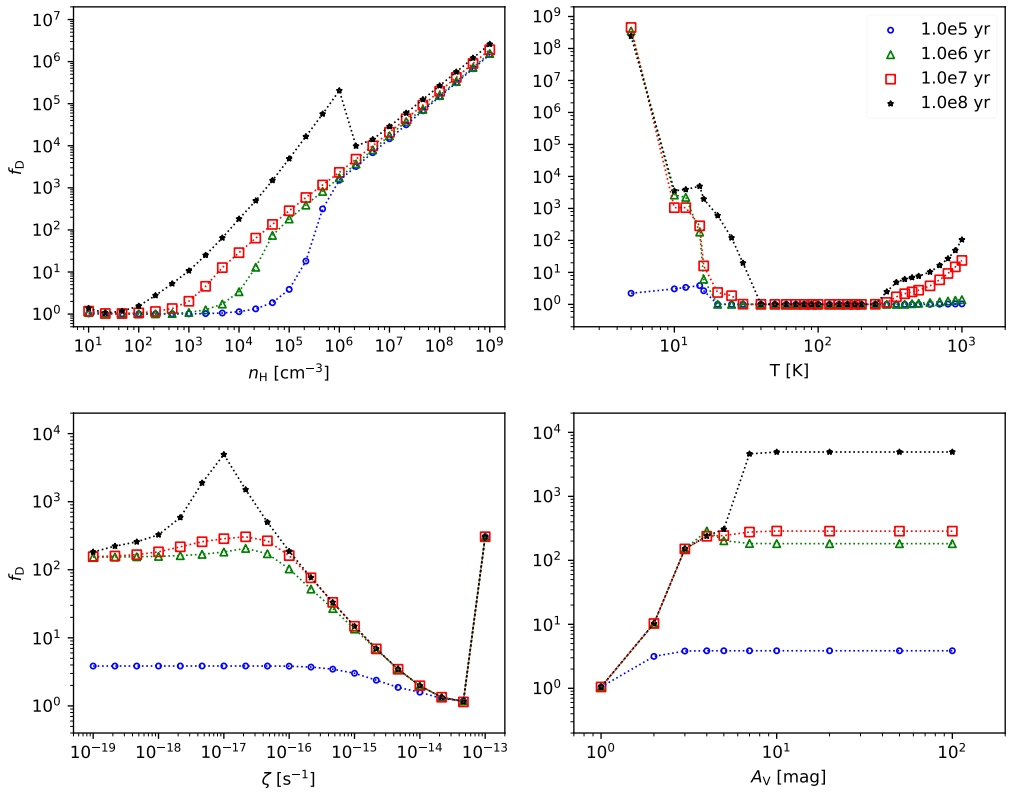

Figure 2.2: CO depletion factor, f_D, evaluated in astrochemical model Grid 1 at fixed times of 10^5 (circles), 10^6 (triangles), 10^7 (squares) and 10^8 yr (stars) as a function of the environmental variables of: (a) top left - number density of H nuclei, $n_{\rm H}$; (b) top right - temperature, T; (c) bottom left - cosmic ray ionization rate, ζ; (d) bottom right - visual extinction, A_V. In each panel the three remaining variables are held fixed at their fiducial level, i.e., $n_{\rm H} = 10^5$ cm^{-3}, $T = 15$ K, $\zeta = 10^{-17}$ s^{-1}, $A_V = 100$ mag.

In the following, we define f_D via:

$$f_D(t) = \frac{1.4 \times 10^{-4}}{X[\mathrm{CO}](t)}, \tag{2.1}$$

where 1.4×10^{-4} is the initial gas phase abundance of CO with respect to H nuclei in our models (i.e., assuming all C is in this form) and $X[\mathrm{CO}](t)$ is the actual gas phase abundance of CO with respect to H nuclei, which evolves in time.
To explore the time evolution of f_D and its dependence on density, temperature, CRIR and A_V, we choose a fiducial reference case with $n_{\rm H} = 10^5$ cm^{-3}, $T = 15$ K, $\zeta = 10^{-17}$s^{-1} and $A_V = 100$mag. We then vary each of these variables systematically, while holding the others constant. The results are shown in Figure 2.1a-d). Simple profiles of f_D versus these environmental variables at several fixed times are shown in Figure 2.2a-d). The time evolution of the abundances of CO, HCO^+ and N_2H^+ are shown in Figure 2.3a-d. We now discuss these results in the following four sub-sections.

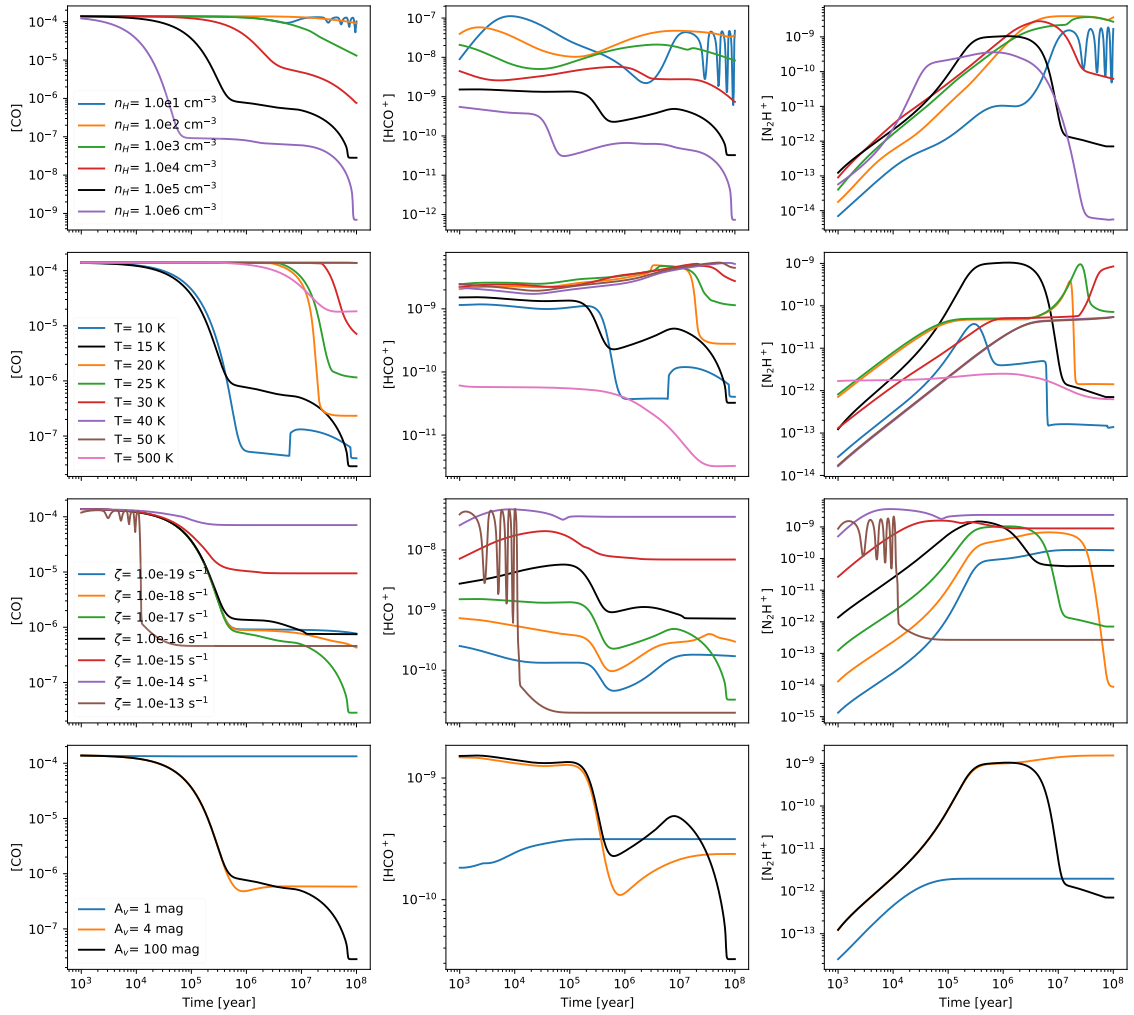

Figure 2.3: Time evolutions of the abundances of CO (left column), HCO^+ (middle column) and N_2H^+ (right column) evaluated in astrochemical model Grid 1, exploring the effects of the environmental variables of: (a) top row - number density of H nuclei, $n_{\rm H}$; (b) second row - temperature, T; (c) third row - cosmic ray ionization rate, ζ; (d) bottom row - visual extinction, A_V. In each row the three remaining variables are held fixed at their fiducial level, i.e., $n_{\rm H} = 10^5\,{\rm cm}^{-3}$, $T = 15\,{\rm K}$, $\zeta = 10^{-17}\,{\rm s}^{-1}$, $A_V = 100$ mag.

2.2.1 Dependence on Density

In the high density regime, $n_{\rm H} \gtrsim 10^5\,{\rm cm}^{-3}$, the general trend shown in Figure 2.1a is that the CO depletion factor increases with time and can reach very high values, $f_D \gtrsim 20$, within a few Myr. As expected, the evolution proceeds more quickly at higher densities, which lead to higher rates of CO molecules hitting and sticking to the dust grains.

At low densities, $n_{\rm H} \lesssim 10^2\,{\rm cm}^{-3}$, the freeze-out rates become very low and the desorption rates are high enough to keep most CO in the gas phase. We note that at these densities and at relatively higher CRIRs ($\gtrsim 10^{-16}\,{\rm s}^{-1}$) (not shown in Figure 2.1a) competing processes that destroy CO, e.g., via interaction with CR-

produced He^+ or CR-induced FUV photons, become more important (note when $A_V = 100$ mag, the destruction of CO via external FUV photons is unimportant). The system can then evolve to having most of the C in atomic or ionized form, and hence the CO abundance is lowered and f_D appears large.
Focusing on the density range that is relevant to IRDCs (at least as averaged on ∼parsec scales), i.e., $n_H \sim 10^4$ to $10^5 cm^{-3}$, we see from Fig. 2.2a that after 100,000 yr f_D is still quite small ($\lesssim 2$) at the low density end of this range, but is rising steeply with density at the high-density end. By 1 Myr, it is still relatively low at the low density end, while at the high-density end of the range it is approaching quasi-equilibrium values of $f_D \gtrsim 100$, which would hold even at ~ 10 Myr. However, as we will see later, this evolution of f_D with time and its dependence on density can be very sensitive to the temperature in the range from ~ 15 to 20 K.

2.2.2 Dependence on Temperature

Time dependant evolutions of f_D at different temperatures are shown in Figures 2.1b and 2.2b. The actual gas phase abundances of CO versus time for these models are shown in Figure 2.3, along with similar evolutions of HCO^+ and N_2H^+. The strong dependence of f_D evolution with T in the range from $\sim 10-50$ K is clearly illustrated, i.e., above this temperature range, gas phase CO remains the main reservoir of C. At temperatures $\gtrsim 500$ K, C is still mostly in the gas phase, but mostly in the form of HCN, rather than CO.

2.2.3 Dependence on Cosmic Ray Ionization Rate

Time dependant evolutions of f_D at different CRIRs are shown in Figures 2.1c and 2.2c. The actual gas phase abundances of CO versus time for these models are shown in Figure 2.3c, along with similar evolutions of HCO^+ and N_2H^+. In this figure, we sometimes see oscillations in the abundances of CO, HCO^+ and N_2H^+ at early times, i.e., in the models with high CRIR and where the condition $10^{18}\ cm^{-3}\ s < n_H/\zeta < 2.2 \times 10^{18}\ cm^{-3}\ s$. Such behaviour has been noted in the previous study of Maffucci et al. (2018), corresponding to the High Ionization Phase (HIP) case discussed by Roueff and Le Bourlot (2020). More generally, the results of Figures 2.1c and 2.2c indicate that as ζ increases, CO depletion begins earlier in time, but reaches a lower equilibrium value. A different mode of evolution occurs at the highest value of CRIR ($\zeta = 10^{-13}\ s^{-1}$), in which C is mostly in the form of C^+.

2.2.4 Dependence on Visual Extinction

Time dependant evolutions of f_D at different levels of A_V are shown in Figures 2.1d and 2.2d. The actual gas phase abundances of CO versus time for these models are shown in Figure 2.3d, along with similar evolutions of HCO^+ and N_2H^+. These figures show that in the models with $A_V > 5$ mag, CO evolution has little dependency on the level of visual extinction so that CO depletion becomes large after about 1 Myr, no matter the value of A_V.

3

Observational Data and Abundance Estimates

3.1 Molecular Line Data

The rotational transitions listed in Table 3.1 were mapped toward the IRDC G28.37+00.07 (hereafter Cloud C, Butler & Tan 2009; 2012) in August 2008, May 2013 and September 2013 using the IRAM (Instituto de Radioastromía Milimétrica) 30m telescope in Pico Velata, Spain. Observations were performed in On-The-Fly mode with map size 264×252; central coordinates $\alpha = 18^h42^m52.3^s$, $\delta = -4°0226.2$; and a relative off position of $(-370, 30)$. An angular separation in the direction perpendicular to the scanning direction of 6 was adopted.
The VESPA receiver was utilised for observations of $C^{18}O(1-0)$ and $N_2H^+(1-0)$, which provided a spectral resolution of 20 kHz, corresponding to a velocity resolution of 0.053 and 0.063 km s^{-1}, respectively. The other species were observed using the FTS spectrometer with 200 kHz resolution, corresponding to velocity resolutions of $\sim$ 0.4 to 0.7 km s^{-1}. In the worst case, i.e., at the lowest frequency of 81.5 GHz, the angular resolution of the molecular line data has a HPBW of 32 (corresponding to 0.78 pc at the 5 kpc distance of the IRDC). Peak intensities were measured in units of antenna temperature, $T_A^\star$, and converted into main-beam temperature, $T_{\rm mb}$. Beam and forward efficiencies of 0.73 and 0.95, respectively, for $\nu \sim 145$ GHz, and 0.86 and 0.95 for $\nu \sim 86$ GHz were used. The final data cubes were produced using the CLASS and MAPPING software within the GILDAS package[1].

3.2 Mass Surface Density and Temperature Data

The MIR extinction (MIREX) map of Butler and Tan (2012), derived from 8 μm *Spitzer*-IRAC imaging data, with the NIR correction of Kainulainen and Tan (2013), was used as a first method to estimate the mass surface density, Σ, of selected regions in the IRDC. The advantage of this map is that it has a high angular resolution of 2 and the derivation of Σ does not depend on the temperature of the cloud. The disadvantages of the map are that it cannot make a measurement in regions that are MIR bright. Furthermore, the map saturates at values of $\Sigma \sim 0.5$ g cm^{-2}, i.e., in regions with Σ approaching this value the map underestimates the true value of Σ.

[1] https://www.iram.fr/IRAMFR/GILDAS/

Table 3.1: Observed molecular species, rest frequencies, rotational quantum numbers of the transitions, rotational constants, rotational partition function, Einstein A coefficients, energy of lower state, degeneracy of upper state, velocity resolution, $B_{\rm eff}$ and HPBWs.

molecule	ν (GHz)	J	B (Hz)	$Q_{\rm rot}(T_{\rm ex}$=7.5K)	A (s^{-1})	E_L (K)	g_u	dv (kms^{-1})	$B_{\rm eff}$	θ()
$HC^{18}O^+$	85.1621570	1-0	4.26e10	3.90	3.6450E-05	0.00	3	0.6876	0.81	28.89
$H^{13}CO^+$	86.7542884	1-0	4.34e10	3.83	3.8539E-05	0.00	3	0.6749	0.81	28.36
$HN^{13}C$	87.0908500	1-0	4.35e10	3.82	2.3840E-05	0.00	3	0.6723	0.81	28.25
HNCO	87.9250443	4-3	1.11e10	36.90	8.7801E-06	6.33	9	0.6659	0.81	27.98
HCN	88.6304160	1-0	4.43e10	3.88	8.0884E-06	0.00	3	0.6606	0.81	27.76
N_2H^+	93.1761300	1-0	4.66e10	3.71	3.6300E-05	0.00	3	0.0628	0.80	26.40
$C^{18}O$	109.7821734	1-0	5.49e10	3.11	6.2661E-08	0.00	3	0.0533	0.78	22.41
CH_3OH	145.1031850	3-2	2.47e10	13.25	1.2323E-05	6.96	7	0.4035	0.73	16.95
H_2CO	145.6029490	2-1	3.88e10	10.52	7.8127E-05	3.49	5	0.4021	0.73	16.90

An independent measure of Σ for the IRDC has been derived by Lim et al. (2016) based on *Herschel*-PACS and SPIRE sub-mm emission imaging data, with this analysis also simultaneously yielding an estimate of the dust temperature. These maps have an angular resolution of 18 for the Σ map and 36 for the T map, i.e., much lower than that of the MIREX map. As discussed by Lim et al. (2016), there are significant effects due to Galactic plane foreground and background emission that contaminate the emission arising from the IRDC itself. In our analysis, we make use of the map derived from the Galactic Gaussian (GG) foreground-background subtraction method.

3.3 Ten Selected IRDC Regions

From the final data cubes, we extracted molecular line spectra from ten regions in the IRDC (see Figure 3.1). Each region has a circular aperture of radius 16, which was set so that the angular resolution of the HPBW of the lowest frequency transition, i.e., from $HC^{18}O^+(1-0)$, fits within the region. At the 5 kpc distance of the IRDC, the radius of each region corresponds to 0.39 pc.

The locations of the ten positions were selected for having relatively high values of Σ and for having a range of star formation activities. In particular, positions P1 to P6 (shown with red circles in Figure 3.1) are known to be sites of active star formation based on the presence of CO outflows (Kong et al., 2019) and containing *Herschel*-Hi-GAL 70 μm point sources (Moser et al., 2020). However, these positions are still dark structures at 8 μm: indeed the P1 to P6 positions correspond approximately to the MIREX Σ peaks of C1, C2, C4, C5, C6 and C8, respectively, identified and characterised by Butler and Tan (2012).

The positions from P7 to P10 (shown with black circles in Figures 3.1 and 3.2) are not directly associated with massive condensations previously identified within the cloud (Rathborne et al., 2006; Butler and Tan, 2009,0) and have been selected for being relatively quiescent in terms of their star formation activity (Kong et al., 2019;

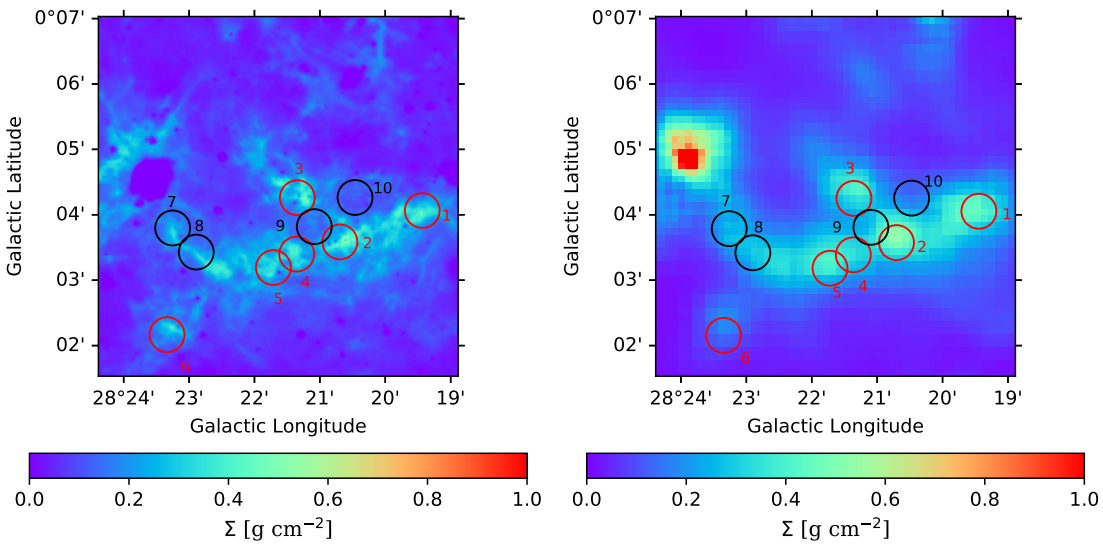

Figure 3.1: (a) Left: MIREX derived mass surface density map of IRDC G28.37+00.07 from Kainulainen and Tan (2013) (scalebar is in g cm^{-2}). The ten regions selected for our astrochemical study are marked with circles, labelled 1 to 10. Regions 1 to 6 (red) are known to harbor some star formation activity, while regions 7-10 have been specifically selected to avoid known protostellar sources. (b) Right: Sub-mm emission derived mass surface density map of the IRDC from Lim et al. (2016) using the Galactic Gaussian method of foreground-background subtraction (scalebar is in g cm^{-2}). Note, it is of significantly lower angular resolution than the MIREX map (see text). The analysed positions are marked as in (a).

Moser et al., 2020).

From the two mass surface density maps shown in Figure 3.1, we have measured the average values of $\Sigma_{\rm MIREX}$ and $\Sigma_{\rm sub-mm}$ in each of the ten regions P1 to P10 (see Table 3.2). This also allows an estimate of $N_{\rm H}$, assuming a mass per H of $\mu_{\rm H} = 1.4 m_{\rm H} = 2.34 \times 10^{-24}$ g (i.e., approximately due to $n_{\rm He} = 0.1 n_{\rm H}$ and ignoring contributions from other species). We assume an uncertainty of ∼30% in the measurements of Σ and $N_{\rm H}$ (Kainulainen and Tan, 2013; Lim et al., 2016).

We have then estimated the average total amount of visual extinction, A_V, through each region using the standard dust model assumptions of Kainulainen and Tan (2013), i.e.,

$$N_{\rm H} = 1.9 \times 10^{21}\ {\rm cm}^{-2} \left(\frac{A_{V,{\rm tot}}}{\rm mag} \right). \tag{3.1}$$

However, we then divide this estimate of the total extinction through the region by a factor of 4 in order to obtain an estimate of the typical extinction from the nearest boundary of the IRDC, i.e., $\bar{A}_V = A_{V,{\rm tot}}/4$.

We have estimated the average number density of H nuclei, $n_{\rm H}$, in each region by assuming the material is distributed in a spherical volume with radius equal to the circular aperture radius of the region projected on the sky. These values are also listed in Table 3.2.

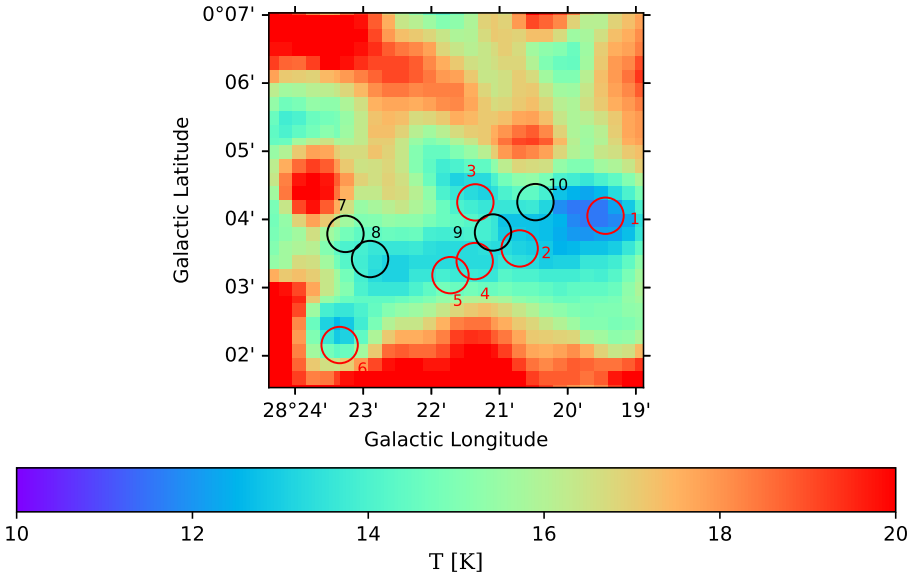

Figure 3.2: Sub-mm emission derived dust temperature map of IRDC G28.37+00.07 from Lim et al. (2016) using the Galactic Gaussian method of foreground-background subtraction (scalebar in K). The ten regions selected for our astrochemical study are marked with circles, labelled 1 to 10, as in Fig. 3.1.

Finally, by using the dust temperature map from Lim et al. (2016), we have estimated the Σ-averaged T values for the ten selected positions (Figure 3.2). These values are also listed in Table 3.2. The uncertainties in T are assumed to be at the level of 30% (Lim et al., 2016).

3.4 Molecular Abundances

We now estimate column densities of the nine observed species listed in Table 3.1 in the 10 regions of the IRDC and use these results to calculate their abundances with respect to the total H nuclei, i.e., N_X/N_H. For the column density estimation we have used Equation A4 of Caselli et al. (2002):

$$\begin{aligned} N_X &= \frac{8\pi\nu^2}{Ag_uc^3}\frac{k}{h}\frac{1}{J_\nu(T_{\rm ex})-J_\nu(T_{\rm bg})} \\ &\times \frac{Q_{\rm rot}}{1-\exp(-h\nu/[kT_{\rm ex}])}\frac{1}{\exp(-E_L/[kT_{\rm ex}])}\int T_{\rm mb}dv, \end{aligned} \tag{3.2}$$

where ν is the frequency of the observed transition, A is the Einstein coefficient obtained from the CDMS catalog[2], $g_u = 2J+1$ is the statistical weight of the upper level, E_L is the energy of the lower level, and $J_\nu(T_{\rm ex})$ and $J_\nu(T_{\rm bg})$ are the equivalent Rayleigh-Jeans excitation and background temperatures, respectively. For these we set $T_{\rm ex}$= 7.5 K based on the multi-transition CO study of an IRDC by Hernandez

[2]https://cdms.astro.uni-koeln.de/classic/

Parameter	P1	P2	P3	P4	P5	P6	P7	P8	P9	P10
R.A. (J2000)	18:42:46.687	18:42:50.709	18:42:49.490	18:42:52.583	18:42:53.970	18:43:00.610	18:42:54.636	18:42:55.289	18:42:50.591	18:42:47.860
Dec. (J2000)	-4:04:08.830	-4:03:14.763	-4:02:21.514	-4:02:44.647	-4:02:31.320	-4:01:32.639	-4:00:52.451	-4:01:21.835	-4:02:47.469	-4:03:08.458
Σ [g cm^{-2}]	0.394	0.438	0.330	0.322	0.336	0.130	0.239	0.270	0.315	0.171
	0.270	0.296	0.265	0.267	0.259	0.187	0.193	0.195	0.164	0.116
$N_{\rm H}$ [10^{23} cm^{-2}]	1.68	1.87	1.41	1.38	1.44	0.56	1.02	1.15	1.35	0.73
	1.15	1.26	1.13	1.14	1.11	0.80	0.83	0.83	0.70	0.50
$n_{\rm H}$ [10^4 cm^{-3}]	10.50	11.70	8.84	8.65	9.02	3.48	6.39	7.21	8.46	4.58
	7.19	7.88	7.06	7.12	6.94	4.99	5.16	5.21	4.38	3.11
$t_{\rm ff}$ [yr]	1.3×10^5	1.3×10^5	1.5×10^5	1.5×10^5	1.5×10^5	2.3×10^5	1.7×10^5	1.6×10^5	1.5×10^5	2.0×10^5
$A_{V,\rm tot}$ [mag]	88.4	98.4	74.2	72.6	75.8	29.2	53.7	60.5	71.1	38.5
	60.7	66.6	59.6	60.1	58.3	42.1	43.4	43.9	36.9	26.1
$\bar{A}_V$ [mag]	22.1	24.6	18.6	18.2	19.0	7.3	13.4	15.1	17.8	9.6
	15.2	16.6	14.9	15.0	14.6	10.5	10.9	11.0	9.2	6.5
T [K]	11.8	13.1	13.5	13.4	13.8	14.1	14.9	13.6	13.3	13.6
[C^{18}O] [10^{-8}]	4.77±1.47	4.31±1.33	4.86±1.50	5.19±1.60	5.58±1.72	11.00±3.40	6.68±2.06	5.79±1.79	5.13±1.58	6.43±1.98
[CO] [10^{-5}]	1.52±0.56	1.37±0.51	1.54±0.57	1.65±0.61	1.77±0.65	3.51±1.29	2.12±0.78	1.84±0.68	1.63±0.60	2.05±0.75
[H^{13}CO$^+$] [10^{-11}]	1.02±0.31	1.11±0.34	0.87±0.27	0.97±0.30	1.02±0.32	1.52±0.48	0.84±0.26	0.69±0.22	0.96±0.30	1.36±0.42
[HCO$^+$] [10^{-10}]	4.11±1.51	4.48±1.64	3.49±1.28	3.89±1.43	4.10±1.52	6.11±2.27	3.37±1.25	2.77±1.04	3.84±1.41	5.45±2.01
[HC^{18}O$^+$] [10^{-12}]	1.96±0.69	1.84±0.67	1.88±0.74	1.64±0.65	2.19±0.78					1.40±0.36
[HCO$^+$] [10^{-10}]	6.23±2.54	5.84±2.43	5.96±2.64	5.23±2.31	6.98±2.86					4.45±1.45
[N$_2$H$^+$] [10^{-10}]	0.55±0.17	1.79±0.56	1.53±0.47	1.52±0.47	1.10±0.34	2.62±0.81	0.91±0.28	0.80±0.25	1.14±0.35	1.47±0.46
[HN^{13}C] [10^{-11}]	1.41±0.43	1.61±0.50	1.85±0.57	1.64±0.51	1.24±0.39	2.85±0.89	0.94±0.30	0.91±0.29	1.41±0.44	1.88±0.59
[HNC] [10^{-10}]	5.65±2.08	6.47±2.37	7.43±2.73	6.59±2.43	4.97±1.84	11.40±4.24	3.79±1.43	3.67±1.38	5.66±2.09	7.54±2.80
[HCN] [10^{-11}]	11.10±3.44	10.30±3.22	5.86±1.88	8.16±2.57	8.53±2.69	26.60±8.29	10.10±3.28	10.50±3.33	7.66±2.40	10.00±3.32
[HNCO] [10^{-10}]	2.17±0.74	4.29±1.45	4.15±1.41	3.45±1.18	2.74±0.94	1.91±0.72	1.78±0.64	1.40±0.51	3.47±1.18	4.32±1.49
[H$_2$CO] [10^{-11}]	3.89±1.26	10.40±3.33	7.33±2.37	7.66±2.47	6.98±2.25	3.31±1.19	2.76±0.94	2.19±0.73	9.16±2.95	9.94±3.21
[CH$_3$OH] [10^{-9}]	0.52±0.18	1.73±0.60	1.74±0.61	1.33±0.46	1.26±0.44	0.49±0.18	0.45±0.16	0.33±0.12	1.54±0.54	1.93±0.67

Table 3.2: Estimated physical properties and molecular abundances of the P1 to P10 positions in IRDC G28.37+00.07.

et al. (2012), while $T_{\rm bg}$=2.73 K from the CMB. Finally, $Q_{\rm rot}$ is the rotational partition function at the assumed $T_{\rm ex}$. For each molecule, $Q_{\rm rot}$ has been calculated by fitting its values from JPL catalogue[3], except in the case of N_2H^+ and HCN for which, since their main rotational transitions split into hyperfine components, the partition function reported in the JPL catalogue includes an additional factor and it does not coincide with the pure rotational partition function. Hence, for N_2H^+

[3]https://spec.jpl.nasa.gov/ftp/pub/catalog/catdir.html

		XR	UR	R
		$[\zeta/t/n_{\rm H}/T/A_V/\chi^2]$	$[\zeta/t/n_{\rm H}/T/A_V/\chi^2]$	$[\zeta/t/n_{\rm H}/T/A_V/\chi^2]$
P1	Case 1	1.0e-18/1.70e5/1.0e5/15/20/0.11	1.0e-18/1.70e5/1.0e5/15/50/0.11	1.0e-19/2.00e7/2.2e4/20/5/0.10
	Case 2	4.6e-18/1.26e7/1.0e5/15/20/56.95	1.0e-18/1.00e8/2.2e5/20/10/37.75	4.6e-18/1.00e8/1.0e6/30/50/8.56
P2	Case 1	2.2e-18/2.00e5/1.0e5/15/20/0.69	1.0e18/4.17e5/4.6e4/15/50/0.17	2.2e-19/2.24e6/1.0e4/15/5/0.02
	Case 2	2.2e-17/4.47e6/1.0e5/15/20/60.82	1.0e-16/1.45e5/2.2e5/10/10/42.64	1.0e-17/5.62e7/1.0e6/30/50/16.26
P3	Case 1	2.2e-18/1.95e5/1.0e5/15/20/0.97	1.0e-18/3.98e5/4.6e4/15/10/0.49	2.2e-19/2.09e6/1.0e4/15/5/0.17
	Case 2	1.0e-17/6.92e6/1.0e5/15/20/66.17	2.2e-18/5.25e7/2.2e5/20/10/47.71	4.6e-18/1.00e8/1.0e6/30/50/18.56
P4	Case 1	2.2e-18/1.91e5/1.0e5/15/20/0.86	1.0e-18/3.89e5/4.6e4/15/10/0.31	2.2e-19/2.00e6/1.0e4/15/5/0.03
	Case 2	1.0e-17/6.92e-17/1.0e5/15/20/64.20	2.2e-18/5.13e7/2.2e5/20/10/43.41	4.6e-18/1.00e8/1.0e6/30/50/15.68
P5	Case 1	2.2e-18/1.74e5/1.0e5/15/20/0.48	1.0e-18/3.55e5/4.6e4/15/10/0.21	4.6e-19/7.59e5/2.2e4/15/5/0.13
	Case 2	1.0e-17/7.24e6/1.0e5/15/20/64.38	2.2e-18/5.13e7/2.2e5/20/10/43.08	4.6e-18/1.00e8/1.0e6/30/50/12.58
P6	Case 1	4.6e-18/2.88e5/4.6e4/15/7/2.47	1.0e-18/7.24e5/2.2e4/15/5/1.73	4.6e-19/1.66e6/1.0e4/15/5/1.33
	Case 2	4.6e-17/2.51e5/4.6e4/15/7/53.73	4.6e-19/1.48e7/2.2e4/20/5/13.31	4.6e-19/1.48e7/2.2e4/20/5/13.31
P7	Case 1	1.0e-18/3.31e5/4.6e4/15/10/0.72	2.2e-19/8.32e5/2.2e4/15/20/0.39	1.0e-19/2.00e6/1.0e4/15/7/0.21
	Case 2	2.2e-18/2.45e7/4.6e4/15/10/58.95	1.0e-18/1.00e8/1.0e5/20/7/39.32	4.6e-18/1.00e8/1.0e6/30/50/11.61
P8	Case 1	4.6e-19/3.80e5/4.6e4/15/10/0.43	2.2e-19/8.13e5/2.2e4/15/7/0.27	1.0e-19/1.95e6/1.0e4/15/5/0.04
	Case 2	2.2e-18/2.45e7/4.6e4/15/10/55.88	1.0e-19/7.76e6/2.2e4/15/7/37.03	4.6e-18/1.00e8/1.0e6/30/50/12.06
P9	Case 1	2.2e-18/1.78e5/1.0e5/15/20/0.48	1.0e-18/3.63e5/4.6e4/15/10/0.27	1.0e-19/2.34e6/1.0e4/15/100/0.12
	Case 2	1.0e-17/7.08e6/1.0e5/15/20/63.83	2.2e-18/5.13e7/2.2e5/20/10/44.47	4.6e-18/1.00e8/1.0e6/30/50/13.95
P10	Case 1	2.2e-18/3.16e5/4.6e4/15/10/0.51	4.6e-19/7.94e5/2.2e4/15/20/0.20	2.2e-19/1.91e6/1.0e4/15/100/0.06
	Case 2	4.6e-18/1.38e7/4.6e4/15/10/60.40	2.2e-17/5.01e5/4.6e4/10/7/38.31	4.6e-18/1.00e8/1.0e6/30/50/14.36

Table 3.3: Extracted Astrochemical parameters of the best models in Restricted (R), Ultra restricted (UR) and Extra restricted (XR) regions, using observed abundances of [CO],[HCO^+] and [N_2H^+] as Case 1, and all observed abundances as Case 2. The extracted parameters are ζ [s^{-1}], Time [year], n_H [cm^{-3}], T [K], A_V [mag] and χ^2, respectively from left to right. For the Case 2 in Extra restricted region (XR), we have excluded the models with higher ζ (>1.0e-14 s^{-1}). Hence the models which could give us early time solution (<1.0e4 years) were eliminated in consequence.

and HCN, we have calculated $Q_{\rm rot}$ as:

$$Q_{\rm rot} = \sum_{J=0}^{\infty} (2J+1) \exp\left(\frac{-E_J}{kT_{\rm ex}}\right), \tag{3.3}$$

where, $E_J = J(J+1)hB$ is the energy of the J level and B is the rotational constant of the molecule. The various parameters used to derive the abundances of the species are listed in Table 3.1. Finally, we note that $N_{N_2H^+}$ and N_{HCN} obtained from Equation 3.2 have been corrected for the transition statistical weights of 0.11 and 0.3333, respectively, since only one of the hyperfine lines was used in each case to derive total abundances.

In deriving column densities from the observed spectra, which are shown in Figures 3.3 and 3.4, we must make a choice of the velocity range over which to integrate the line intensities. From inspection of the spectra, this range is chosen to have a common extent of 77 to 82 km s^{-1}, motivated by the goal of covering the dense gas tracers of $H^{13}CO^+(1-0)$, $HC^{18}O^+(1-0)$ and $N_2H^+(1-0)$. Examining the spectra of Figures 3.3 and 3.4, we see that $C^{18}O$(1-0) generally shows emission from several components that span a broader velocity range than the above dense gas tracers. In our analysis, we will only measure the CO column density from the part of $C^{18}O$(1-0) emission that falls in the velocity range from 77 to 82 km s^{-1}.

To estimate the uncertainties in the total column densities, we consider the following factors. First is the uncertainty in the integrated intensity of each line, which we assess to be equal to the noise integrated in a line-free spectral range and calculated as:

$$\int T_{\rm mb,noise} dv = \sqrt{n} \Delta T_{\rm mb,noise} dv \tag{3.4}$$

where n is the number of channels, each of velocity width dv, that are summed in the integration and $\Delta T_{\rm mb,noise}$ is the noise in an individual channel.

Second is the systematic uncertainty due to the need to assume a value of $T_{\rm ex}$. We note that $T_{\rm ex} = 7.5$ K has been adopted for all the species. If $T_{\rm ex}$ is varied by $\pm 30\%$ about this value, the estimated total column density changes by $\sim 7-28\%$. For most species, this systematic error dominates over that due to the noise in the integrated intensity. In our analysis, we estimate the overall uncertainty in total column densities by summing the above two sources of uncertainties in quadrature. However, we note that there are other potential sources of systematic error, such as the assumption that the emission in the particular chosen velocity range is a good representation of the physical component of the molecular cloud that is being modelled.

For some of the species, like CO, HCO^+ and HNC, the column density is estimated by conversion from a rarer isotopologue. This involves another source of systematic uncertainty. For these conversions, we assume $[^{12}C]/[^{13}C] = 40.2 \pm 8.0$ (Zeng et al., 2017) and $[^{16}O]/[^{18}O] = 318 \pm 64$ (Hezareh et al., 2008) and these levels of uncertainty are also propagated in quadrature for the final column density estimate.

We note that, since no significant signal is detected for the $HC^{18}O^+$(1-0) transition toward the positions P6, P7, P8, P9, and P10, we have estimated their $HC^{18}O^+$ column density from the average of their spectra. Then, we have apportioned this column density among the five positions in proportion to their H column densities.

The final step of the analysis is to estimate abundances of species with respect to H nuclei that are assumed to be present in the same molecular cloud component. For this we simply divide the above estimates of total species column density by the estimate of H nucleus column density obtained previously either via *Herschel*-observed sub-mm dust emission or via MIR extinction. Each of these methods is

assumed to have a 30% uncertainty, which is summed in quadrature for the final abundance estimate. The obtained results are summarised in Table 3.2. Note, the H column densities obtained by both methods are themselves quite similar (see above) and, for simplicity, in the remaining analysis we will adopt those estimates based on the sub-mm dust continuum emission.

Figure 3.3: Spectra of observed species at positions P1-P5. The dashed lines indicate the velocity range 77 to 82 km s^{-1}, which has been selected to cover the dense gas as traced by N_2H^+ and $H^{13}CO^+$. In the left column panels, the amplitudes of the signals of $H^{13}CO^+(1-0)$, $HC^{18}O^+(1-0)$ and $N_2H^+(1-0)$ have been multiplied by a factor of three for clarity of display.

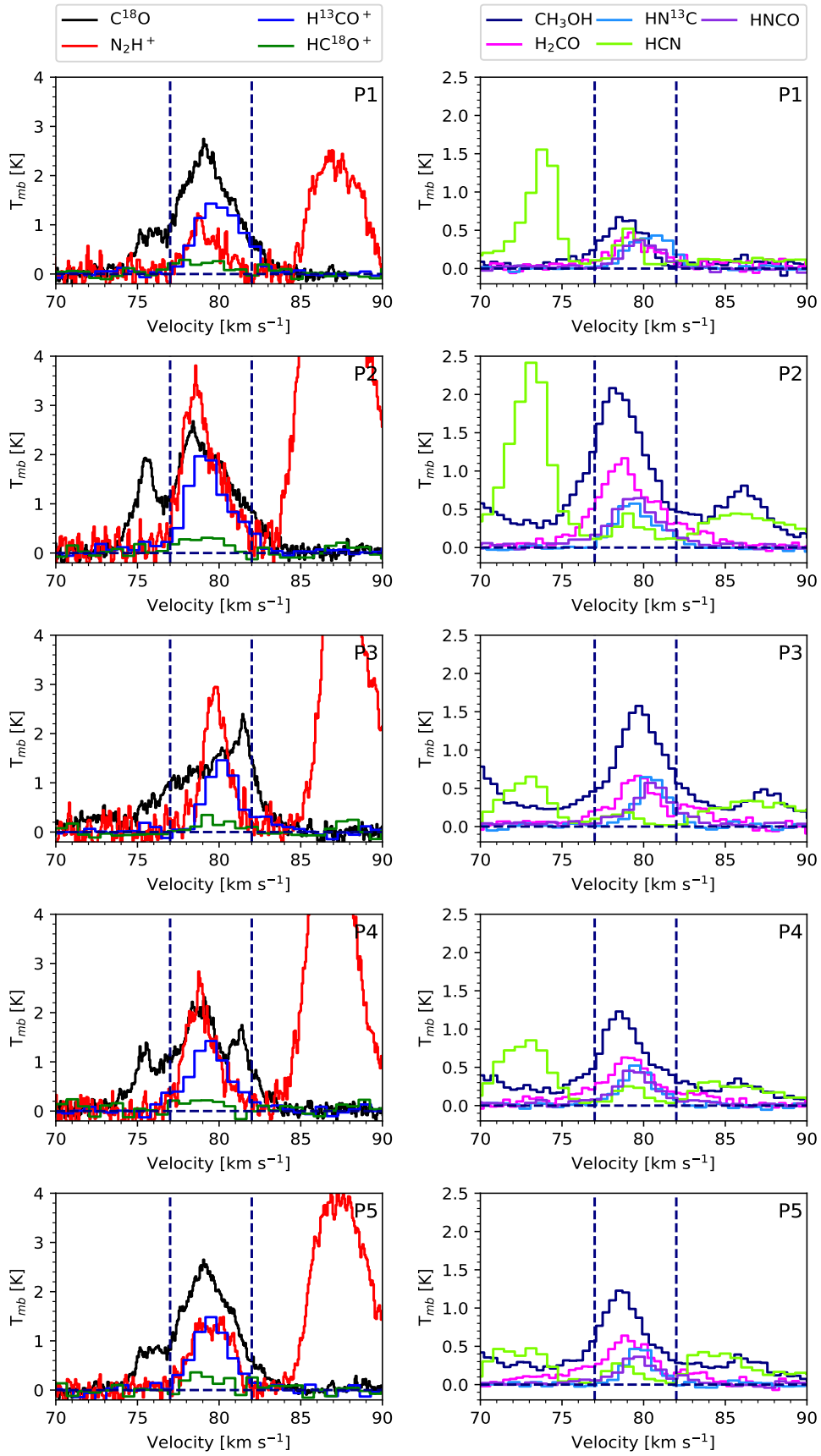

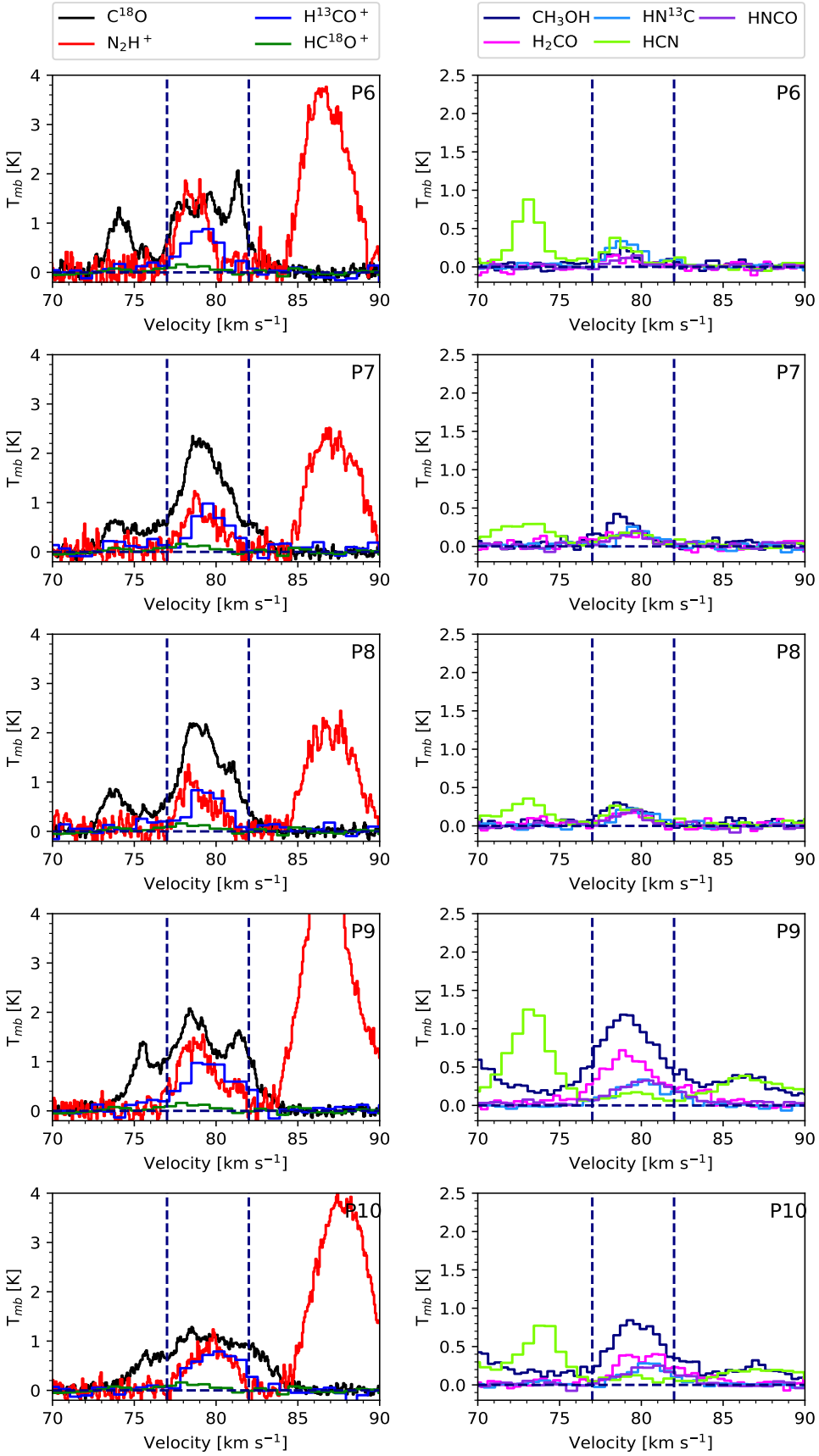

Figure 3.4: As Fig. 3.3, but now for positions P6-P10.

4

Results

4.1 Abundances, including density dependence

Here we summarise the abundances of the various species obtained in the IRDC positions (see also Table 3.2). For CO, we find a typical value of [CO] $\equiv N_{\rm CO}/N_{\rm H} \sim 2 \times 10^{-5}$, which corresponds to a CO depletion factor of $f_D \sim 7$. In Figure 4.1a we plot f_D versus $n_{\rm H}$, which reveals a trend of increasing depletion factor (i.e., smaller gas phase CO abundance) with increasing density. While correlated uncertainties are present in the measurements of f_D and $n_{\rm H}$ (estimated via $N_{\rm H}$), the trend is significant, given a Pearson correlation coefficient of $r = 0.93$. For completeness, the same information about the trend of [CO] with $n_{\rm H}$ is also shown in Figure 4.2a, with this figure showing the abundances versus density for all eight species measured in our study.

Theoretically, for a given set of conditions, including cloud age, one expects higher CO depletion factors at higher densities, i.e., due to higher rates of freeze-out leading to shorter freeze-out timescales. To illustrate this quantitatively, Figure 4.1a shows some example models of the time evolution of f_D versus $n_{\rm H}$, with other parameters set to values of $T = 15$ K, $A_V = 20$ mag, and three values of $\zeta = 10^{-18}$, 10^{-17} and 10^{-16} s^{-1} explored. The observed trend of f_D versus $n_{\rm H}$ can be explained by a model in which the 10 positions have fairly similar ages of 2×10^5 yr. We note that this result is quite insensitive to certain choices of the astrochemical models, such as ζ, A_V (for values > 5 mag) and T (for values < 20 K). However, as we discuss below, certain choices in the models about how nonthermal desorption processes are implemented can have impact on the inferred chemical age from these data.

Figure 4.1b plots f_D versus $\bar{A}_V$. While we see a trend of increasing observed f_D versus $\bar{A}_V$, we note that $\bar{A}_V \propto N_{\rm H} \propto n_{\rm H}$. At a given age and volume density, the astrochemical models do not predict a significant variation of f_D with A_V (at least for $A_V > 5$ mag, which is the relevant range). Thus, we consider that trend we observe here is more likely to be caused by variations in density in the regions.

For HCO^+, using emission from $H^{13}CO^+$ we infer typical abundances of [HCO^+] $\sim 4 \times 10^{-10}$. The abundances inferred from $HC^{18}O^+$ are systematically larger by about 30%. However, such a difference is within the isotopologue ratio uncertainties. While the two lowest density regions, P6 and P10, are seen to have the highest abundances, $\sim 6 \times 10^{-10}$, the overall correlation with density is not as strong as in the case of [CO] (see Figure 4.2b).

We estimate [N_2H^+] $\sim 10^{-10}$ on average (see Figure 4.2c). Again, the lowest density region has the highest abundance, but, as with HCO^+, there is no significant trend

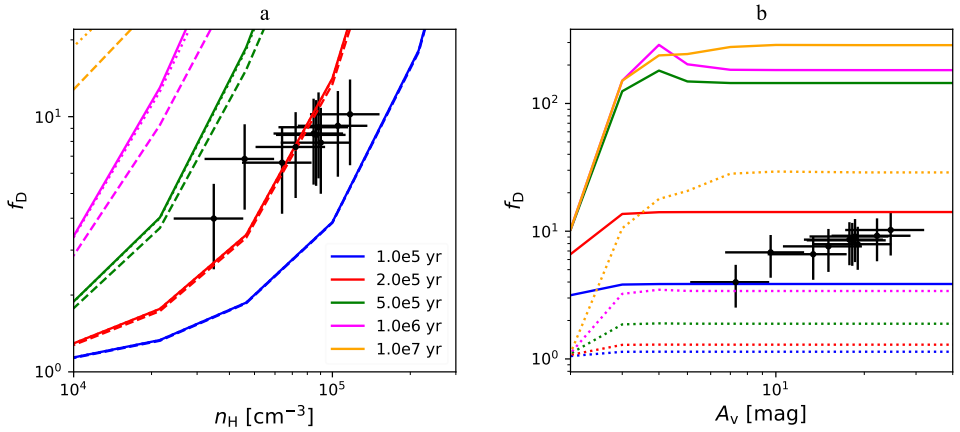

Figure 4.1: *(a) Left:* CO depletion factor (f_D) versus number density of hydrogen nuclei ($n_{\rm H}$). The data for each position are shown, along with their uncertainties. Astrochemical models are shown for ages ranging from 10^5 yr to 10^7 yr and for $\zeta = 10^{-18}\,{\rm s}^{-1}$ (dotted lines) and $10^{-17}\,{\rm s}^{-1}$ (solid lines) and $10^{-16}\,{\rm s}^{-1}$ (dashed lines) with other parameters set to be $T = 15$ K and $A_V = 20$ mag. *(b) Right:* CO depletion factor (f_D) versus visual extinction (A_V). The data for each position are shown, along with their uncertainties. Astrochemical models are shown here for $n_{\rm H} = 10^5$ cm^{-3}, $T = 15$ K and $\zeta = 10^{-17}\,{\rm s}^{-1}$ with solid lines (colors represent different times, as in legend of (a)). An equivalent model for $n_{\rm H} = 10^4\,{\rm cm}^{-3}$ is shown with dotted lines.

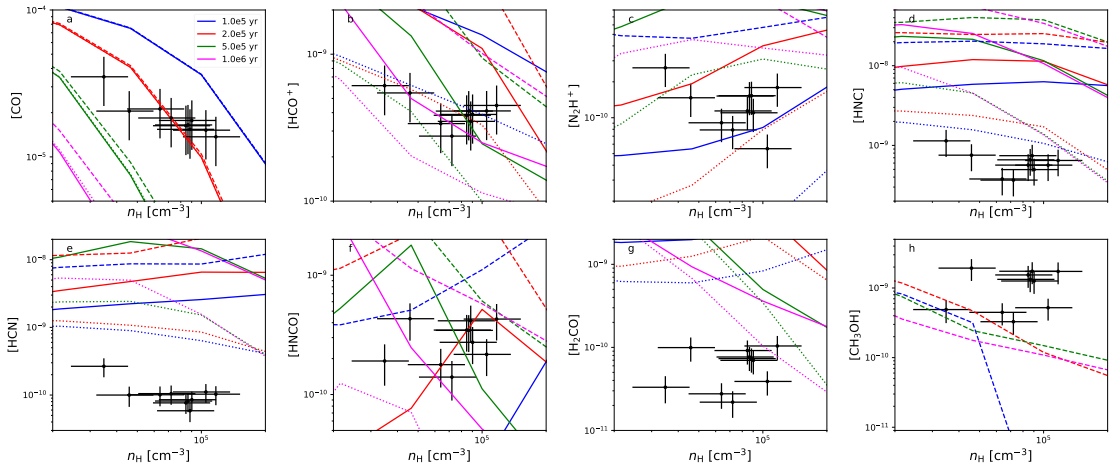

Figure 4.2: Observed abundances of (a) CO, (b) HCO^+, (c) N_2H^+, (d) HNC, (e) HCN, (f) HNCO, (g) H_2CO and (h) CH_3OH versus $n_{\rm H}$. Astrochemical model results are also shown for $\zeta = 10^{-18}\,{\rm s}^{-1}$ (dotted lines), $10^{-17}\,{\rm s}^{-1}$ (solid lines) and $10^{-16}\,{\rm s}^{-1}$ (dashed lines) with other parameters set to be $T = 15$ K and $A_V = 20$ mag.

with density. Similar results are seen for HNC, with typical abundance of 6×10^{-10} (Fig. 4.2d) and HCN, with typical abundance of [HCN] $\sim 10^{-10}$ (Fig. 4.2e).
Finally, we find [HNCO]$\sim 3 \times 10^{-10}$, [H_2CO]$\sim 5 \times 10^{-11}$ and [CH_3OH]$\sim 10^{-9}$ as

typical values (see Fig. 4.2f, g and h). Here there are hints of a bifurcation in the regions, with P1, P6, P7 and P8 having relatively low values, and the other six regions having abundances that are several times larger.
We note that P7 and P8 were specifically chosen to be in regions that are relatively quiescent with respect to star formation activity as traced by CO(2-1) outflows (Kong et al., 2019), while still containing relatively dense structures. P1 also includes the candidate C1-N and S massive pre-stellar cores (Tan et al., 2013), i.e., significant quantities of dense, quiescent gas, although there are also two protostellar sources (C1-Sa and C1-Sb) in the same region. P6 also appears to be quiescent, e.g., not containing a 70 μm detected protostar (Moser et al., 2020), but is outside the region mapped for CO(2-1) outflows. Thus, we tentatively conclude that regions with relatively low star formation activity also have relatively low abundances of the relatively complex species of HNCO, H_2CO and CH_3OH. Such a result could be due to requirement of protostellar warming or outflow shock activity to liberate these species efficiently from dust grain ice mantles.

4.2 Astrochemical Implications for Cosmic Ray Ionization Rate and Cloud Age

In this section we use the abundance measurements of the IRDC positions to constrain conditions in the clouds, especially ζ and t, via the astrochemical models described in §2. In general we will compare a set of the observed abundances, $[X_i]_{\rm obs}$, in a given position with those of theoretical model abundances, $[X_i]_{\rm theory}$. We will search the model grid parameter space $(n_{\rm H}, T, A_V, \zeta, t)$ to minimize a χ^2 metric of the following form

$$\chi^2 = \sum_i W_i[(\log_{10}[X_i]_{\rm obs} - \log_{10}[X_i]_{\rm theory})/\log_{10}(\sigma_i)]^2, \tag{4.1}$$

where σ_i is an estimate of the uncertainty in the abundance, including the basic observational uncertainty and any allowed theoretical model uncertainty, and W_i is a weighting factor, which allows certain species to be given greater or lesser importance in the analysis.

4.2.1 Constraints using [CO], [HCO^+] and [N_2H^+] (Case 1)

As first step (Case 1), we only consider the abundances of CO, HCO^+ (obtained from $H^{13}CO^+$) and N_2H^+, i.e., CO and the two molecular ions in our set of species. We have first searched the entire model grid parameter space to find best fitting models and map out the χ^2 landscape. However, unrealistic solutions can be found with low values of χ^2, e.g., at high temperatures ($\gtrsim$ 500 K), where low values of [CO] are caused by gas-phase chemical processing of the CO, rather than by CO freeze out onto dust. Thus, we focus on a restricted (R) search over the ranges: $n_{\rm H} = 10^4 - 10^6$ cm^{-3}; $T = 10 - 50$ K and $A_V = 5 - 100$ mag. We also consider ultra-restricted (UR) searches in which $n_{\rm H}$ and A_V are set to the closest values in the model grid to those of the observed region and with only adjacent values also

considered. For this UR case we limit the search to $T = 10 - 20\,\mathrm{K}$. Finally, we have an extreme-restricted (XR) case where we only search the ζ-t parameter space in the best physically matched model for n_H, A_V and T (note, in this case we always set $T = 15\,\mathrm{K}$: this is always the closest match, except for P1, where $T = 11.8\,\mathrm{K}$, but even here, for simplicity, we will consider 15 K for the XR case).
The χ^2 landscape in the ζ versus t plane for the XR search at the P2 position (i.e., with $n_\mathrm{H} = 1.0 \times 10^5\,\mathrm{cm}^{-3}$, $A_V = 20\,\mathrm{mag}$ and $T = 15\,\mathrm{K}$) with Case 1 ([CO], [HCO^+] and [N_2H^+]) fitting is shown in the central panel of Figure 4.3. The surrounding eight panels show the effect on the χ^2 landscape of stepping in the model grid to the next higher and lower values of density and temperature, while keeping A_V held fixed at 20 mag.
We notice several main features in Figure 4.3. First, the best result in the central panel that is matched to the physical conditions of P2 has $\zeta = 2.2 \times 10^{-18}\,\mathrm{s}^{-1}$ and $t = 2 \times 10^5\,\mathrm{yr}$ and yields a value of $\chi^2 = 0.69$. These values are listed in Table 3.3, along with those obtained for the UR and R searches.
Second, we see that this position of lowest χ^2 sits in an "island" that extends to higher values of ζ at earlier times and lower values of ζ at later times. There is also a separate, secondary island of relatively low values of χ^2 at later times and higher ζ, with local minimum at $t = 2.82 \times 10^6\,\mathrm{yr}$ and $\zeta = 2.2 \times 10^{-16}\,\mathrm{s}^{-1}$.
As we vary the density of the model, the above features are broadly preserved, with a shift in the best position to earlier times and higher ζ if the density is raised, and later times and lower ζ if it is lowered. We have also inspected the equivalent figures for the cases with $A_V = 10$ and 50 mag and find only modest differences compared to the $A_V = 20\,\mathrm{mag}$ cases. Considering temperature variation, the models at $T = 10\,\mathrm{K}$ have a similar structure, with the best position now at moderately higher values of ζ, but with worse values of χ^2. However, at $T = 20\,\mathrm{K}$ the results are quite different, with the previous best χ^2 island now erased and the new best solutions being at much later times, with the best value unrealistically old.
To understand the above behaviour, we next consider the detailed time evolution of some example models from the XR conditions: we examine the overall best model and the best model in the secondary, late-time island (see Fig. 4.4). With a temperature of 15 K, for both models the evolution of gas-phase CO abundance is initially one of monotonic decline due to freeze-out onto dust grains. At the XR density of $n_\mathrm{H} = 2.2 \times 10^5\,\mathrm{cm}^{-3}$, this reaches the observed depletion factor of ~ 10 by about $2 \times 10^5\,\mathrm{yr}$, independent of ζ. The influence of the CRIR is seen on the (quasi-)equilibrium level of gas phase CO abundance that is reached, i.e., after about 1 Myr. However, even in the case with $\zeta = 2.2 \times 10^{-16}\,\mathrm{s}^{-1}$, this abundance of CO is about 10 times smaller than the observed level. Thus the process of CO freeze-out essentially sets the timescale of the best model.
Next, considering the abundance of HCO^+, it is seen to have a fairly constant evolution in time. In the overall best model it is gradually declining in the first few hundred thousand years. Finally, the evolution of [N_2H^+] shows an early-time rapid rise from very low values associated with our assumed initial conditions, i.e., all N in atomic form. The rate of this rise is more rapid when ζ is higher. This is followed by a plateau phase and subsequent decline in abundance. The overall best model is achieved on the first time rise of [N_2H^+], while the higher CRIR later-time

model is achieved on the decline from the plateau phase. It is $[HCO^+]$ and $[N_2H^+]$ that mostly set the CRIR of the best model, in particular favoring a low value of $\zeta = 2.2 \times 10^{-18}\,s^{-1}$. This is illustrated in Fig. 4.5, where models with ten times higher and lower values of CRIR compared to this value are shown.

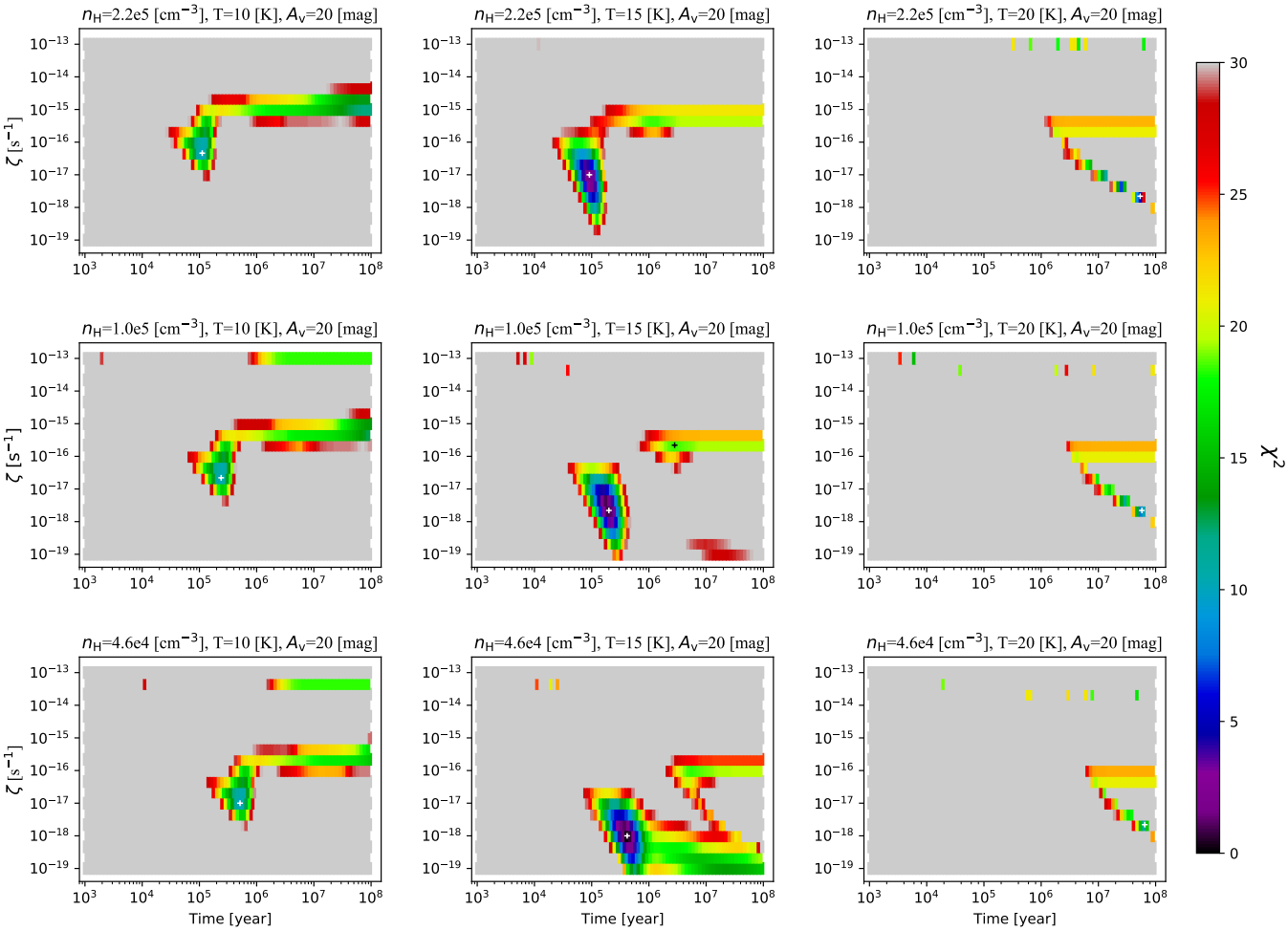

Figure 4.3: The central panel shows the χ^2 landscape (up to values of 30) in the ζ versus t plane for the P2 position for the XR search (i.e., with $n_H = 1.0 \times 10^5\,cm^{-3}$, $A_V = 20$mag and $T = 15$K) Case 1 (fitting to abundances of CO, HCO^+ and N_2H^+). The location of the minimum χ^2 is marked with a white cross. The surrounding eight panels show the effect on the χ^2 landscape of stepping in the model grid to the next higher and lower values of density and temperature (as labelled). Note, A_V is held fixed at 20 mag in all these panels (so these are just a subset of the UR search).

Next we consider the results of the UR and R search results for P2. As mentioned, the best fitting models for these search ranges are also listed in Table 3.3. Figure 4.6 shows the projected χ^2 landscapes in the ζ versus t plane for XR, UR and R searches. We see that the regions of low values of χ^2 expand, as expected. The early-time, low-ζ island expands to cover a broader range of times, with the later time solutions being those of lower density and vice versa. In particular, the overall best models are now moved to these later time, lower density, lower ζ regions. However, it should be

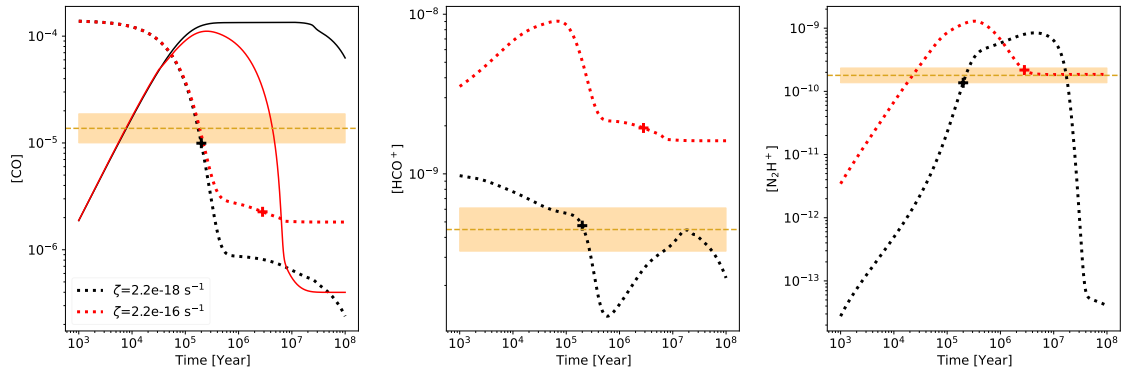

Figure 4.4: Time evolution of [CO] (gas [dotted] and ice [solid] phases) (left), [HCO^+] (middle) and [N_2H^+] (right) for the overall best fitting model (black lines, $\zeta = 2.2 \times 10^{-18}\,s^{-1}$) and best "late-time" model (red lines, $\zeta = 2.2 \times 10^{-16}\,s^{-1}$) for the XR search of the P2 clump, i.e., with $n_H = 1.0 \times 10^5\,cm^{-3}$, $A_V = 20$ mag and $T = 15$ K. The time of the best models along each of these tracks is marked with a "+" symbol. Horizontal dotted lines show the observed values of abundances, with the uncertainties shown by the shaded bands.

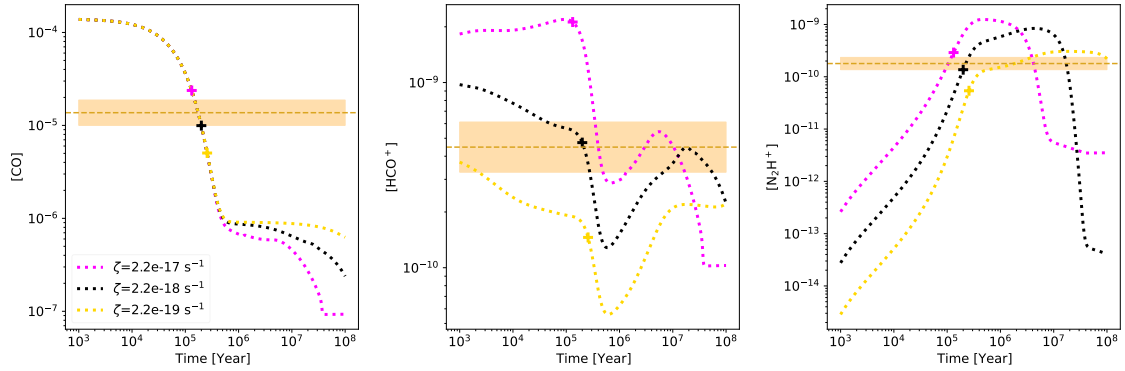

Figure 4.5: As Figure 4.4, but now showing the effect of varying the CRIR by a factor of 10 to higher (magenta) and lower (yellow) values compared to the XR best model value of $\zeta = 2.2 \times 10^{-18}\,s^{-1}$. The best timescales for each of the models are shown with corresponding "+" symbols, given the observed abundances of the P2 location.

noted that there are quite widespread regions of relatively low χ^2, so the relevance of the particular overall best model is less significant.

Next we consider the Case 1 results for the rest of the IRDC positions. In particular, we next consider the P6 position (Fig. 4.7), which has been selected to be starless. We see that the overall feature of the χ^2 distributions for P6 are quite similar to those of P2. The equivalent figures for the other regions follow the same general patterns and we do not present them here. In general, all these regions also exhibit quite similar χ^2 landscapes for their XR, UR and R Case 1 search results.

Thus, in summary, the main features of the Case 1 fitting are that the best solutions

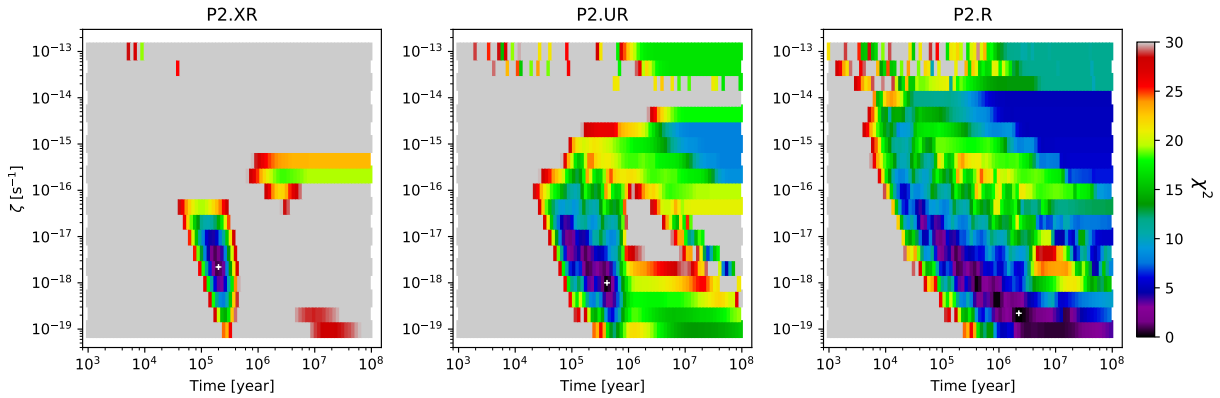

Figure 4.6: The projected best χ^2 values in the ζ versus t plane for the P2 position for the XR (left), UR (middle) and R (right) search methods with Case 1 (fitting to abundances of CO, HCO^+ and N_2H^+). The location of the minimum χ^2 is marked with a white cross in each panel.

have relatively low CRIRs ($\sim 10^{-18}$s^{-1}) and yield ages in the range $\sim 10^5$ to $\sim 10^6$yr. There is an extended "valley" of low χ^2 values extending to higher CRIR solutions (e.g., $\sim 10^{-17}$ s^{-1}), but requiring smaller ages (e.g., 10^5 yr). This type of solution is based on the gas being in a phase of early CO freeze-out, i.e., with the age set by the time needed to freeze-out from the adopted initial conditions of all CO in gas phase.
However, as we will discuss later in §5, we consider that there are caveats with this interpretation. In particular, it seems to be unlikely that all the 10 selected positions would be in this initial phase of CO freeze out and the implied values of CRIR are relatively low compared to previous estimates in the more diffuse ISM. We will thus also discuss possible ways in which later-time solutions ($t \gtrsim 1$ Myr) can be achieved.

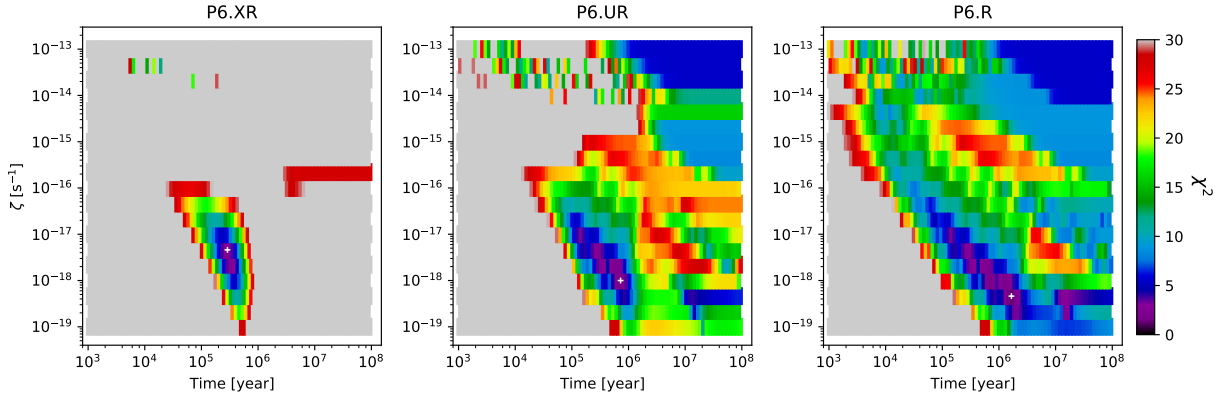

Figure 4.7: As Fig. 4.6, but now for P6.

4.2.2 Constraints using all species (Case 2)

We next show the equivalent results for constraining the astrochemical conditions when the abundances of all the eight species observed at the P2 position are used, which we refer to as Case 2. However, for these additional five species we set their weights to only contribute 25% of the total weighting of χ^2, i.e., 5% each. This choice is made given that we consider that these species have somewhat more uncertain astrochemistry and that, being neutral species, they have a less direct connection to the CRIR than HCO^+ and N_2H^+.

The Case 2 χ^2 landscape in the ζ versus t plane for the XR search at the P2 position (i.e., with $n_{\rm H} = 1.0 \times 10^5$ cm^{-3}, $A_V = 20$ mag and $T = 15$ K) is shown in the central panel of Figure 4.8. The surrounding eight panels show the effect on the χ^2 landscape of stepping in the model grid to the next higher and lower values of density and temperature, while keeping A_V fixed at 20 mag.

We notice several main features in Figure 4.8. First, the best result in the central panel that is matched to the physical conditions of P2 has $\zeta = 2.2 \times 10^{-17}$ s^{-1} and $t = 4.47 \times 10^6$ yr and yields a value of $\chi^2 = 60.82$. These values are listed in Table 3.3, along with those obtained for the UR and R searches. We see that this position of lowest χ^2 sits close to the later-time, higher CRIR region that was found as a secondary solution area in the Case 1 XR search. The previous best χ^2 region from Case 1 that is at earlier times and lower CRIRs is still seen in Case 2 as a local minimum of χ^2, but now does not contain the global minimum. We note also that for Case 2 the overall values of χ^2 are much greater than for Case 1. We examine below the reason for the poorer level of fitting.

As we vary the density of the model, the general, overall shape of the χ^2 landscape does not change too much, however, we note that going to higher densities leads to the best fit model being at earlier times ($\sim 10^5$ yr) and with relatively high CRIR ($\zeta = 2.2 \times 10^{-16}$ s^{-1}). This solution region is also found when the temperature is lowered to 10 K. When raising the temperature to 20 K we see that later time solutions are preferred, with there being some overlap of these with the best region found in the XR case. Similar to Case 1, having inspected the equivalent results for $A_V = 10$ and 50 mag, we find only modest differences compared to the $A_V = 20$ mag cases.

To understand the above behaviour, we next consider the detailed time evolution of some example models from the XR conditions. First, we examine the overall best model (see Fig. 4.9). As seen before in Case 1, with a temperature of 15 K, the evolution of gas-phase CO abundance is initially one of monotonic decline due to freeze-out onto dust grains. At the XR density of $n_{\rm H} = 1.0 \times 10^5$ cm^{-3}, this reaches the observed depletion factor of ~ 10 by about 2×10^5 yr. However, because of the abundance of other species, especially CH_3OH, later time solutions are preferred, even though the gas-phase abundance of CO is now in worse agreement compared to the observed value. We also see why the overal value of χ^2 is worse, since the abundances of several of the species, such as CO, HNC, HCN, H_2CO and CH_3OH, are not very well fit even for the best model, with differences greater than a factor of 10.

A comparison of models with different CRIRs is shown in Fig. 4.10, where models with ten times higher and lower values of ζ compared to that of the best XR model

are shown. In general higher values of ζ lead to higher abundances of the considered species and vice versa.
Next we consider the Case 2 UR and R search results for P2. As mentioned, the best fitting models for these search ranges are also listed in Table 3.3. Figure 4.11 shows the projected χ^2 landscapes in the ζ versus t plane for XR, UR and R searches. We see that the regions of low values of χ^2 expand, as expected. In the UR search, a solution at earlier time and higher CRIR is preferred, which is in a region already seen in Fig. 4.8. In the less constrained R search, a solution with an unrealistically old age ($\gg 10^7$ yr) is found, although earlier times with only moderately worse χ^2 values are apparent. In general, the estimated values of ζ via Case 2 at P2 are higher than those found in Case 1. Later time solutions are also more favored. However, the overall fits are worse, with larger values of χ^2.
Next we consider the Case 2 results for the rest of the IRDC positions. In particular, we next consider the P6 position (Fig. 4.12). There are some noticeable differences in the Case 2 χ^2 landscapes of P6 compared to P2, especially for the XR and UR searches. For XR in P6 there is a greater preference for earlier time solutions, while for UR a later time solution is favored. The equivalent figures for the other regions are quite similar and we do not present them here.
Thus, in summary, the main features of the Case 2 fitting are that, compared to Case 1, the best solutions have relatively larger values of CRIRs ($\sim 10^{-17}\,\mathrm{s}^{-1}$) and a more extended range of ages, from $\sim 10^5$ to $\sim 10^7$ yr. However, the overall goodness of the fits is worse.

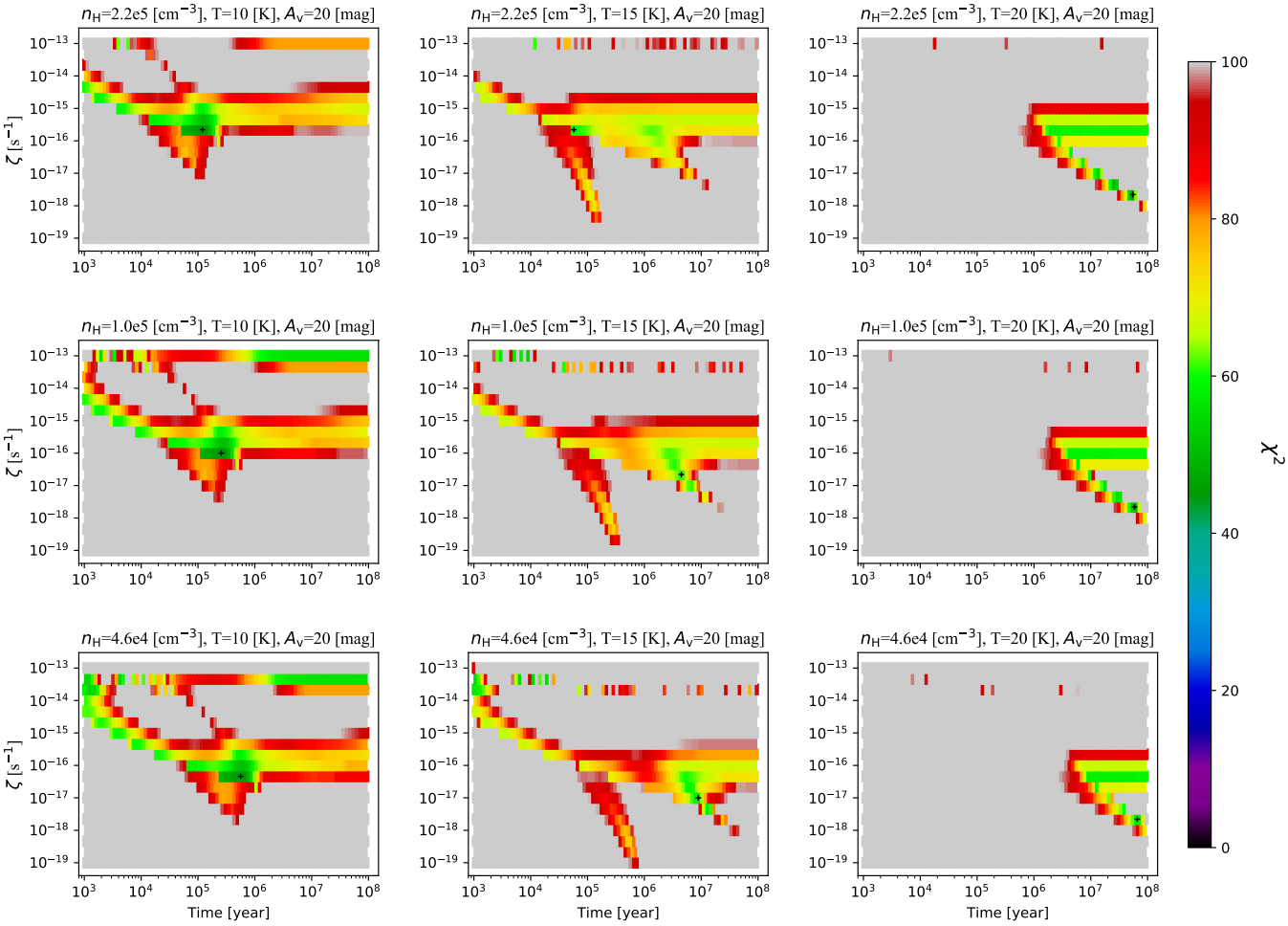

Figure 4.8: The central panel shows the χ^2 landscape (up to values of 100) in the ζ versus t plane for the P2 position for the XR search (i.e., with $n_{\rm H} = 1.0 \times 10^5\,{\rm cm}^{-3}$, $A_V = 20$ mag and $T = 15$ K) Case 2 (fitting to abundances of all species). The location of the minimum χ^2 is marked with a black cross. The surrounding eight panels show the effect on the χ^2 landscape of stepping in the model grid to the next higher and lower values of density and temperature (as labelled). Note, A_V is held fixed at 20 mag in all these panels (so these are just a subset of the UR search).

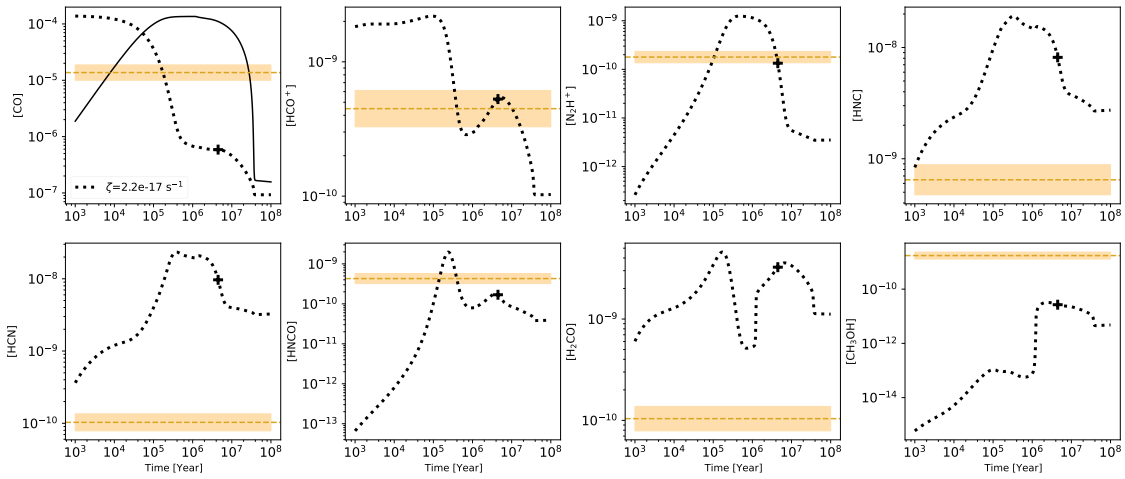

Figure 4.9: Time evolution of [CO] (gas [dotted] and ice [solid] phases) (top left). The remaining panels show the equivalent panels for the gas phase abundances of the rest of the species for the overall best fitting model ($\zeta = 2.2 \times 10^{-17}$ s^{-1}), for the XR search of the P2 clump, i.e., with $n_{\rm H} = 1.0 \times 10^5$ cm^{-3}, $A_V = 20$ mag and $T = 15$ K. The time of the best overall model along each of these tracks is marked with a "+" symbol. Horizontal dotted lines show the observed values of abundances, with the uncertainties shown by the shaded bands.

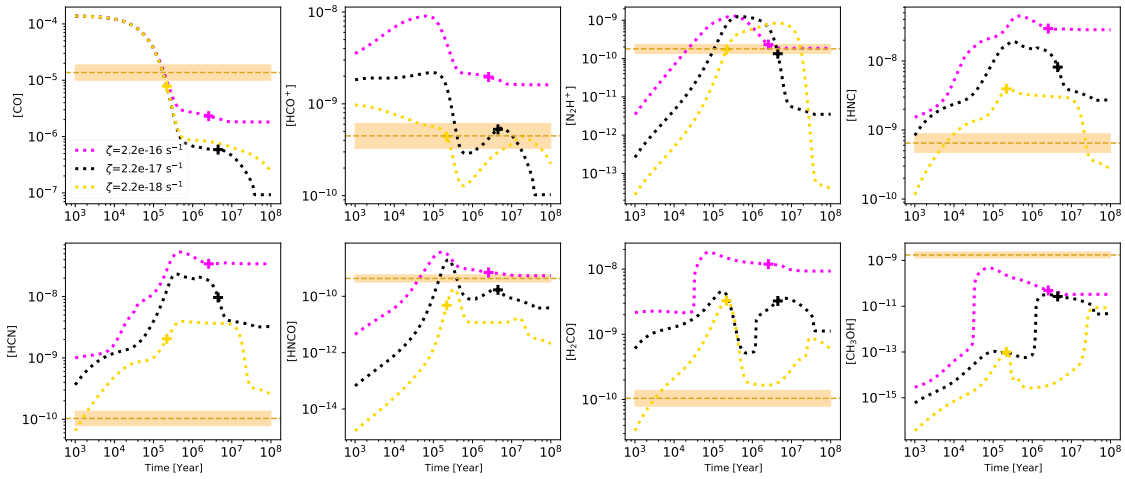

Figure 4.10: As Figure 4.9, but now showing the effect of varying the CRIR by a factor of 10 to higher (magenta) and lower (yellow) values compared to the XR best model value of $\zeta = 2.2 \times 10^{-17}$ s^{-1}. The overall best timescales for each of the models are shown with corresponding "+" symbols, given the observed abundances of the P2 location.

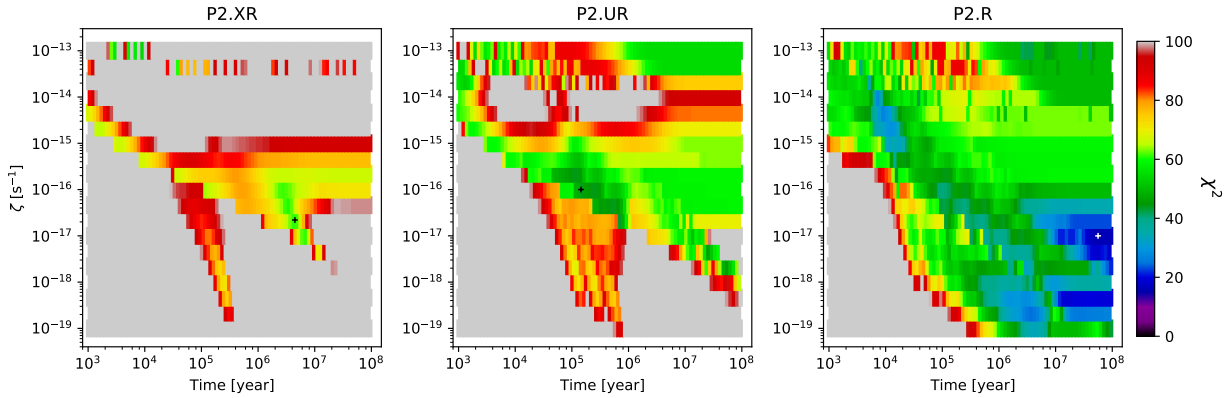

Figure 4.11: The projected best χ^2 values in the ζ versus t plane for the P2 position for the XR (left), UR (middle) and R (right) search methods with Case 2 (fitting to abundances of all species). The location of the minimum χ^2 is marked with a black or white cross in each panel.

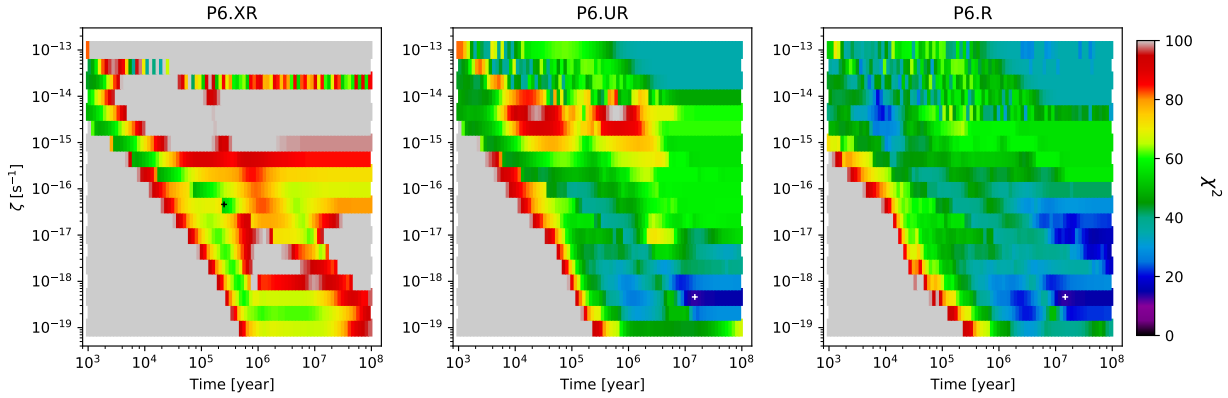

Figure 4.12: As Fig. 4.11, but now for P6.

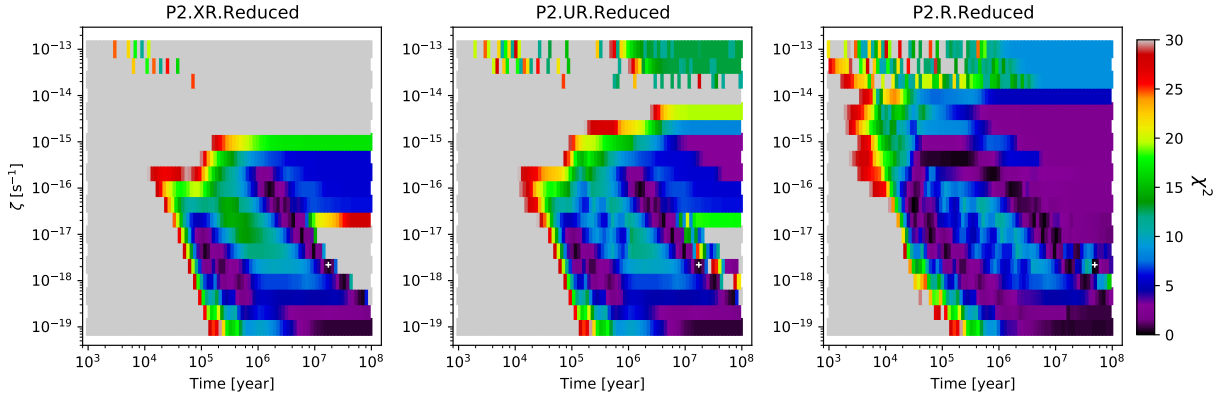

Figure 4.13: Investigation of effect of CO envelope contamination showing the projected best χ^2 values in the ζ versus t plane for the P2 position for the XR (left), UR (middle) and R (right) search methods with Case 1 (fitting to abundances of CO, HCO^+ and N_2H^+). For this fitting, the observed abundance of CO has been reduced by a factor of 10 and the associated uncertainty is set to be a factor of 3. The location of the minimum χ^2 is marked with a white cross in each panel.

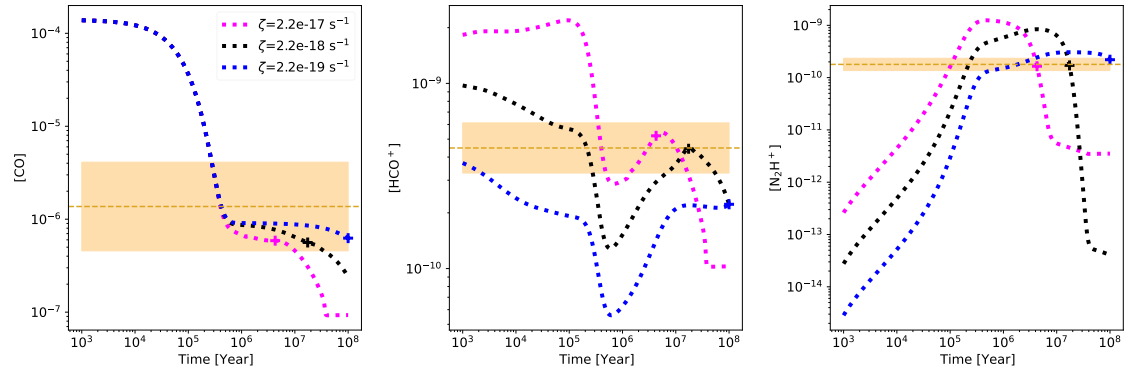

Figure 4.14: Investigation of effect of CO envelope contamination showing time evolution of [CO] (left), $[HCO^+]$ (middle) and $[N_2H^+]$ (right) for the overall best fitting model (black line, $\zeta = 2.2 \times 10^{-18}$ s^{-1}). Here the observed CO abundance has been reduced by a factor of 10 and the total uncertainty set to be a factor of 3. The effects of varying the CRIR by a factor of 10 to higher (magenta) and lower (blue) values compared to the XR best model value are shown. The best timescales for each of the models are marked with corresponding "+" symbols.

5

Discussion and Extended Analysis

Here we investigate the effects of several aspects of the observational analysis and astrochemical modeling that may have a major influence on the fiducial Case 1 results of a preference for relatively early time ($\sim 10^5$ yr) and low ζ ($\sim 10^{-18}$ s^{-1}) solutions. We consider that such young ages are questionable because it is unlikely that all 10 regions, P1 to P10, are in such early evolutionary stages with ages similar to their current local free-fall times, $t_{\rm ff} = (3\pi/[32G\rho])^{1/2} \sim 10^5$ yr (see Table 3.2). Furthermore, the derived values of CRIR are significantly lower than those derived from previous studies (see §1).

5.1 Contamination by envelope CO emission

CO(1-0) has a much lower critical density than HCO^+(1-0) and N_2H^+(1-0). While we have made efforts to restrict the velocity range used to estimate the CO column density to closely match that of the higher density tracers, it remains possible that our measurement suffers from contamination from lower density, envelope gas that is surrounding the region of interest, but overlapping in velocity space. To account for this possibility and to investigate its potential effects, we simply assume a contamination level of 90%, and reduce the observed CO column density by a factor of 10 (and we set the uncertainty in CO abundance to then be a factor of 3).
Figure 4.13 presents XR, UR and R χ^2 projections in the ζ versus t plane for P2 with this reduced gas phase CO abundance. We find that later-time solutions are now favoured. For example, the best XR solution has $t \simeq 2\times10^7$ yr and $\zeta \simeq 2\times10^{-18}$ s^{-1}. However, there is also a degeneracy with higher CRIR and earlier times that yield similarly low χ^2 values. Figure 4.14 shows time histories of abundances for several example XR models that illustrate these kinds of solutions. The observed HCO^+ abundance is seen to give a constraint on the CRIR, while that of N_2H^+ helps select models at relatively later times.

5.2 Influence of temperature near the CO sublimation limit

The next aspect we investigate is that of the precise choice of temperature in the range 15 K to 20 K[1]. Within this range there is a dramatic difference in the evolution

[1]This effect is also similar to uncertainties in the precise value of the CO-ice binding energy, which we discuss below in §5.4.

of gas phase CO abundance due to freeze-out on dust grains. Recall also that the early-time solutions found in Case 1 are driven largely by the evolution of CO freeze-out from an initial condition of [CO] $\sim 10^{-4}$ to observed values of $\sim 10^{-5}$ (i.e., CO depletion factor of $f_D \sim 10$).
Figure 5.1 shows the time evolution of the abundances of CO, HCO^+ and N_2H^+ in the fiducial Case 1 modeling of P2 with finer temperature variation from 15 to 20 K. We see that a small difference in adopted temperature, i.e., 16 K compared to 15 K, makes a large difference in the gas phase CO abundance during timescales up to $\sim 10^7$ yr. In particular, the model with $T = 16$ K reaches a quasi equilibrium gas phase CO abundance of $\sim 10^{-5}$ after about 300,000 yr, which then persists at about this level for several Myr. Given the sensitivity of this aspect of the astrochemical model to the choice of T and recognizing the systematic uncertainties in both the CO ice binding energy and the measurement of T in the IRDC, it is conceivable that the IRDC clumps are in this quasi-equilibrium phase.
In Figure 5.2 we show examples of the time evolution of [CO], [HCO^+] and [N_2H^+] at $T = 16$ K for various CRIRs. Later time solutions are possible, although the preferred value of ζ remains relatively low, $\sim 10^{-18}$ s^{-1}, set by [HCO^+]. The full projected Case 1 χ^2 landscapes for P2 with XR, UR and R, but with the temperature always fixed to be $T = 16$ K, are shown in Figure 5.3. Here we see the full extent of these later-time, lower-CRIR solutions.

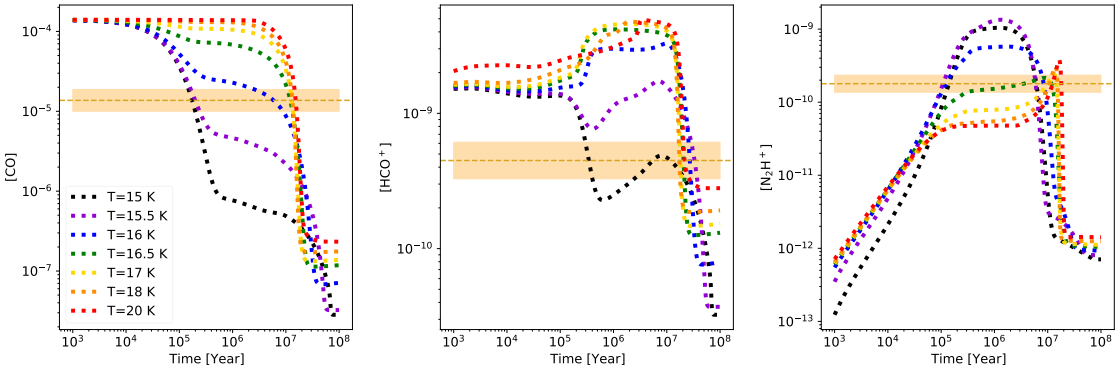

Figure 5.1: Time evolution of [CO], [HCO^+] and [N_2H^+] for XR conditions for P2, i.e., $n_{\rm H} = 1 \times 10^5$ cm^{-3}, A_V =20 mag, but with various temperatures from 15 to 20 K. Here, $\zeta = 1.0 \times 10^{-17}$ s^{-1}. The horizontal band shows the observed abundances, together with corresponding uncertainties, at P2.

5.3 Influence of cosmic ray induced desorption (CRID)

When cosmic rays impact dust grains they cause local heating of the material, which can lead to enhanced thermal desorption of species from the ice mantles. This process has been described by Walsh et al. (2010) and incorporated into the astrochemical network. However, so far, in the fiducial modeling described above,

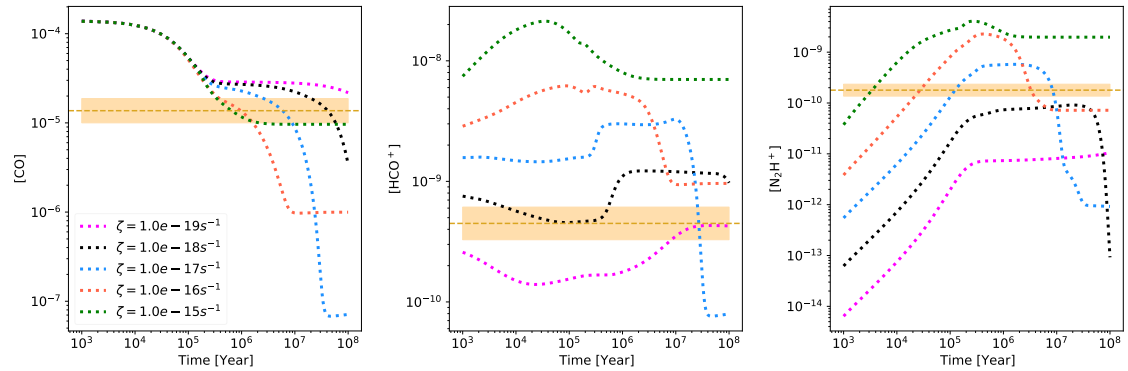

Figure 5.2: Time evolution of CO, HCO^+ and N_2H^+ abundances in the models with $n_H = 1 \times 10^5$ cm^{-3}, $T = 16$ K , $A_V = 100$ mag and for different values of ζ. The horizontal band shows the observed abundances together with corresponding uncertainties at P2.

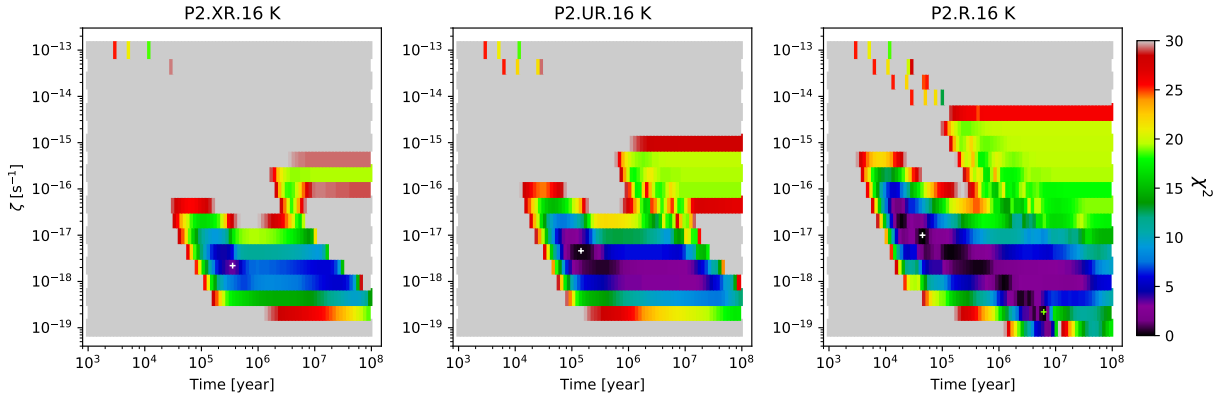

Figure 5.3: Investigation of effect of temperature variation between 15 and 20 K. The panels show the projected best χ^2 values in the ζ versus t plane for the P2 position for the XR (left), UR (middle) and R (right) search methods, but with a further constraint of $T = 16$ K, for Case 1 (fitting to abundances of CO, HCO^+ and N_2H^+). The location of the minimum χ^2 is marked with a white cross in each panel.

we have not included this process due to its inherent large uncertainties. Here we investigate its effects with the standard rates described by Walsh et al. (2010) and Sipilä et al. (2021). In particular, the maximum temperature of the transiently heated grains is assumed to be $T_{CRID} = 70$ K (see §2).
Figure 5.4 shows the results of modeling of [CO], [HCO^+] and [N_2H^+] for XR conditions for P2 with several different values of ζ. For each ζ we show a model with and without CRID, with the latter being the fiducial models already presented. We see that for [CO] the effect of CRID is, as expected, to maintain a higher gas phase abundance, especially from about 0.5 to 10 Myr. As a result of this higher CO abundance, the level of [HCO^+] is also increased in the CRID models.
Figure 5.5 shows the projected χ^2 landscapes in the ζ versus t plane for the Case 1 XR, UR and R search methods for the P2 abundances using models in which CRID

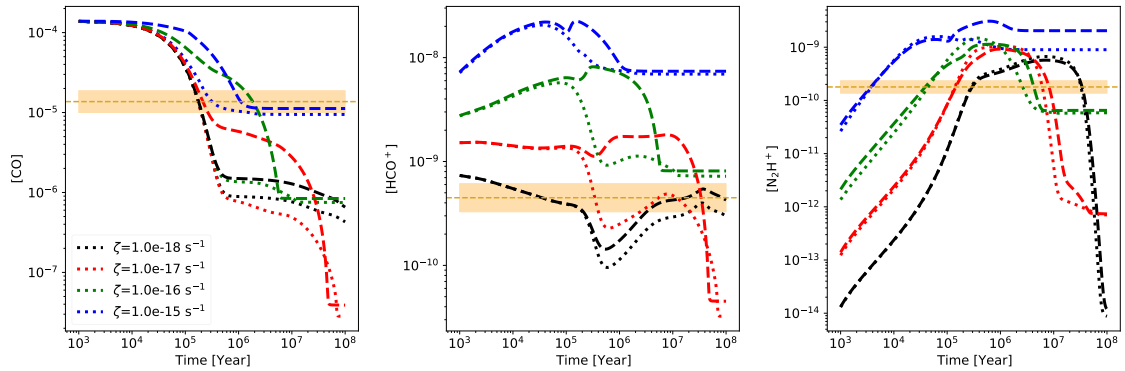

Figure 5.4: Effects of CR induced desorption (CRID). Time evolution of the abundances of the Case 1 species CO (left), HCO^+ (middle) and N_2H^+ (right) in the models with $n_H = 1.0 \times 10^5$ cm^{-3}, $T = 15$ K and $A_V = 20$ mag for several different CRIRs. The dotted lines show the fiducial case in which CRID is not included. The dashed lines show the case in which CRID is included with a standard rate (see text). The horizontal bands show the observed abundances together with their uncertainties at P2.

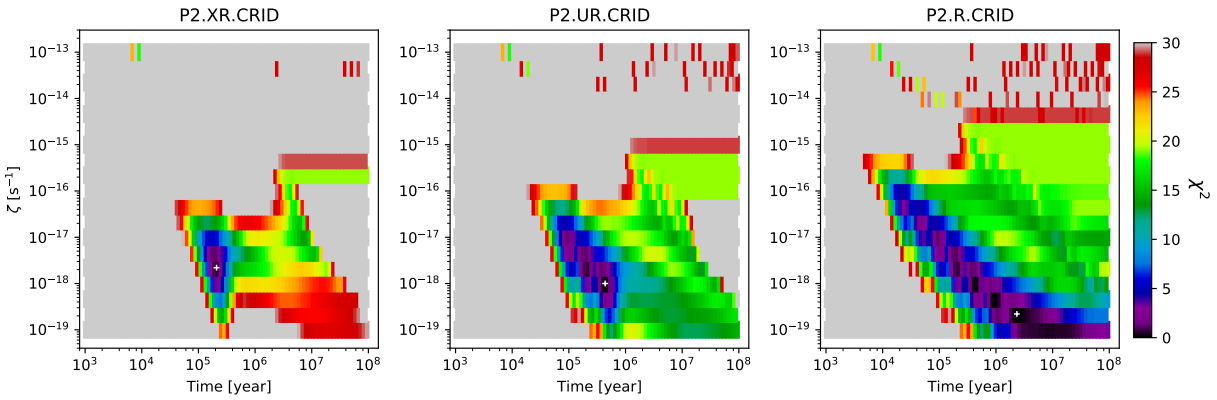

Figure 5.5: Effects of CRID. The panels show the projected best χ^2 values in the ζ versus t plane for the P2 position for the XR (left), UR (middle) and R (right) search methods using models with CRID included for Case 1 (fitting to abundances of CO, HCO^+ and N_2H^+). The location of the minimum χ^2 is marked with a white cross in each panel. Temperature is set to be 15 K for all panels.

is included. While the best overall XR model is similar to that found before without CRID, in general we see that inclusion of CRID raises up the values of χ^2 at later times, i.e., around $t = 1$ Myr.

We conclude that CRID, along with the already investigated effects of CO envelope contamination and intermediate temperatures in the range 15 to 20 K, can make later time and higher CRIR solutions more consistent with the observational constraints of the P2 position (and other IRDC positions). In the next subsection we use the Case 1 data from all the positions, including the observed trends with density, to give some constraints on combinations of these effects that can give reasonable later

time solutions.

5.4 Combined effects and application to the full sample

Here we examine the [CO], [HCO^+] and [N_2H^+] data for all positions P1 to P10 and search for later time (quasi-equilibrium) models, i.e., in the range from $t \sim 0.2$ to 1 Myr, that have CRIRs that are closer to "standard" values, i.e., $\zeta \sim 10^{-17}\,s^{-1}$, to see if they are able to explain the observed trends. Figure 5.6 shows examples of this analysis. In each row the left panel shows f_D versus n_H, the middle panel shows [HCO^+]/[CO] versus n_H, and the right panel shows [N_2H^+]/[CO] versus n_H. In each panel the black points show the observed data of positions P1 to P10. The grey points show the measurements assuming that 90% of the inferred [CO] is contamination from a lower density envelope (i.e., see §5.1). In general we show models for conditions with $A_V = 20$ mag, i.e., a relatively high level of extinction, which should also be applicable for higher values of A_V, and their results at times of 0.1, 0.2, 0.5, 1 and 2 Myr.

The first row of Fig. 5.6 shows models with $\zeta = 2.2 \times 10^{-17}\,s^{-1}$ and with $T = 15$ K (solid lines) and 16 K (dotted lines). The high sensitivity of CO depletion to this choice is clearly seen. Examining the three panels, if the goal is to match the black points, then we see that this is best done at earlier times (~ 0.1 to 0.2 Myr), although the [HCO^+]/[CO] metric is hard to match for any of the models. If the goal is to match the grey points, then this can be done with 15 K models at ages of about 0.2 to 0.5 Myr, although the N_2H^+ abundance can be difficult to match in the highest density sources. If the goal is to find the best later time ($\gtrsim 0.5$ Myr) solution, then it is easiest to do when allowing for some CO envelope contamination, i.e., fitting to grey points, and with the 15 K models. However, overall, in all of these three cases, there is no self-consistent single solution.

The second row of Fig. 5.6 shows models with and without CRID included, with other parameters as in the first row for the 15 K models. If CO envelope contamination is negligible, i.e., attempting to fit black data points, then solutions with relatively young ages are preferred, although there is no global model that gives a good match to all the data. Similarly, if fitting to the grey data points, the models without CRID are preferred, i.e., the same as those found in the analysis of the first row. These are also the best later-time solutions. In summary, these $\zeta = 2.2 \times 10^{-17}\,s^{-1}$ models with CRID at 15 K can only match the data if there is little CO envelope contamination and only at relatively young ages.

The third row of Fig. 5.6 also shows these $\zeta = 2.2 \times 10^{-17}\,s^{-1}$ models with and without CRID, but now for 16 K conditions. We see from the f_D results that there is little scope for CO envelope contamination in these cases and that relatively late time solutions are needed to reach even the minimum CO depletion factor estimates. However, such models tend to overproduce [HCO^+] and [N_2H^+] abundances.

Figure 5.7 presents the same type of results as Fig. 5.6, but now for models with CRIR of $\zeta = 2.2 \times 10^{-18}\,s^{-1}$. It can be seen that the effect of lowering the CRIR is to lower the abundance of HCO^+ and N_2H^+ for a given model as a function of

density and at a given age. This generally gives better agreement with the observed values of [HCO^+]/[CO], and is needed for the case of no CO envelope contamination (black data points).
From a global consideration of the results of Figures 5.6 and 5.7 we draw the following conclusions. First, we note that the observational data for f_D versus density form a very tight relation, especially in comparison to what is seen in the time evolution of many of the models. We consider that this indicates that quasi-equilibrium solutions that converge to this f_D versus $n_{\rm H}$ relation are favored. Furthermore, this argues against there being a significant effect of CO envelope contamination, since this would be expected to introduce scatter in the f_D - $n_{\rm H}$ relation at about the level of the contamination factor. Late time, quasi-equilibrium solutions that match the observed f_D - $n_{\rm H}$ relation can be found, e.g., with 16 K models or with 15 K models with CRID, but to better match [HCO^+] and [N_2H^+] constraints, then relatively low values of CRIR ($\lesssim 2.2 \times 10^{-18}\,{\rm s}^{-1}$) are preferred. There is a strong sensitivity of the normalization of the late-time, quasi-equilibrium f_D - $n_{\rm H}$ relation to temperature occurring at values of temperature close to 15 K. While this means that agreement between the models and the data can be achieved by fine tuning the choice of temperature, again the lack of dispersion in the observational data argues against this solution. Indeed, it would favor a quasi equilibrium solution that is insensitive to temperature, thus pointing to cosmic ray induced desorption mechanisms for liberating CO to the gas phase as being more important than simple thermal desorption.
In the next subsection we consider a chemical network with revised CO ice binding energy and CRID parameters that can yield a reasonable match to the observed constraints, i.e., with later time solutions that converge on the observed f_D - $n_{\rm H}$ relation and that are insensitive to temperature for values below ~ 15 K.

5.5 Models with revised astrochemical parameters of CO ice binding energy and $T_{\rm CRID}$

In the models we have investigated so far, CO ice binding energy was set to the fiducial value of 855 K, leading to a strong sensitivity of CO depletion to temperature variation between 15 and 16 K. While this value of binding energy is suitable for pure CO ice (Öberg et al., 2005), in more realistic situations in which CO is mixed with water ice, its binding energy is expected to increase, with values of ∼1100 K preferred (Öberg et al., 2005; Cuppen et al., 2017). As shown in Figure 5.8, by increasing CO ice binding energy to 1100 K, CO abundance variation between 13 and 16 K becomes negligible, i.e., the gas phase abundance of CO decreases rapidly towards very low values. Thus, to release CO and raise its later-time gas phase abundance closer to observed levels for temperatures in the observed range $\lesssim 15$ K, we need to rely on CRID.
In the astrochemical network, the main parameter which affects significantly the final CRID rate is $T_{\rm CRID}$, i.e., the maximum temperature reached by grains after suffering a CR impact. Within the network utilised so far, the fiducial value of $T_{\rm CRID} = 70$ K. Figure 5.9 shows the effect of varying $T_{\rm CRID}$ from 70 to 100 K. We see that values of $T_{\rm CRID} \sim 90$ to 100 K are able to sustain CO depletion factors of

about 10 for relatively long timescales, up to ~ 10 Myr. Furthermore, as illustrated in Figure 5.10, in these models the level of CO abundance around the timescales from 0.5 to 10 Myr also depends on the level of CRIR.

Figure 5.11 shows examples of XR fitting of P2 for a grid of models with CO ice binding energy of 1100 K and $T_{\rm CRID} = 100$ K, i.e., "Grid 2". Relatively early time and low CRIR solutions are again found as the best overall models, although good solutions with low χ^2 values are now found extending to later times at similar values of CRIR. The main difference compared to the equivalent Grid 1 results is that these later time solutions do not require much lower values of CRIR.

Now we examine again the [CO], [HCO^+] and [N_2H^+] data for all positions P1 to P10 and search for later-time (quasi-equilibrium) models with CO ice binding energy of 1100 K and different values of $T_{\rm CRID}$. Following the format of Figs. 5.6 and 5.7, Figure 5.12 shows examples of this type of analysis. In each row the left panel shows f_D versus $n_{\rm H}$, the middle panel shows [HCO^+]/[CO] versus $n_{\rm H}$, and the right panel shows [N_2H^+]/[CO] versus $n_{\rm H}$. In each panel the black points show the observed data of positions P1 to P10. The grey points show the measurements assuming that 50% of the inferred [CO] is contaminated (i.e., see §5.1). We show models for conditions with $T = 15$K (although results are relatively insensitive to temperatures near this value) and $A_V = 20$ mag and their results at times of 0.1, 0.2, 0.5, 1 and 2 Myr.

The first row of Figure 5.12 presents a high CRIR case with $\zeta = 1.0 \times 10^{-16}$ s^{-1}. To match the observed f_D-$n_{\rm H}$ relation with later-time solutions requires $T_{\rm CRID} \simeq 80$ to 85 K. However, we see that these models are not good fits to the [HCO^+]/[CO] and [N_2H^+]/[CO] data. The second row shows $\zeta = 1.0 \times 10^{-17}$ s^{-1} models with $T_{\rm CRID} = 90$ and 100 K (the latter being the fiducial Grid 2 value). Again, later-time solutions can match the f_D-$n_{\rm H}$ relation and are now seen to be closer to, but still above, the [HCO^+]/[CO] and [N_2H^+]/[CO] constraints. The third and fourth rows bring the CRIR down to $\zeta = 4.6 \times 10^{-18}$ s^{-1} and $\zeta = 2.2 \times 10^{-18}$ s^{-1}, respectively. Values of $T_{\rm CRID}$ within 100 ± 5 K are displayed. In the third row a models with an age of about 0.5 Myr with $T_{\rm CRID} = 95$ K are a good match to the f_D-$n_{\rm H}$ relation with 50% CO envelope contamination and the [HCO^+]/[CO] versus $n_{\rm H}$ data. It is also within about a factor of two of the [N_2H^+]/[CO] data. Finally, in the fourth row the 0.5 Myr models with $T_{\rm CRID} = 105$ K are a good match to all the constraints provided by the f_D, [HCO^+]/[CO] and [N_2H^+]/[CO] versus $n_{\rm H}$ data (assuming 50% CO envelope contamination).

Thus the conclusion of this analysis is that relatively late-time (~ 0.5 Myr) solutions (i.e., much older than a local free-fall time) exist that are insensitive to the gas temperature (in the relevant range $\lesssim 15$ K) requiring only modest levels of CO envelope contamination (as implied be the relatively low scatter in the f_D-$n_{\rm H}$ relation). However, these solutions require thermal heating of dust grain ice mantles up to $T_{\rm CRID} \sim 100$ K. The models also imply that the cosmic ray ionization rate is a factor a few times smaller than the canonical value of $\zeta = 10^{-17}$ s^{-1}.

5.6 Caveats

One important caveat is the relative simplicity of the astrochemical modeling. In regard to the ability of the models to match [HCO^+] and [N_2H^+] as the main constraint on CRIR, we note that in these presented models HCO^+ is one of the main carriers of the positive charge, i.e., with $[HCO^+]/[e^-] \sim 0.5$. One may consider whether the lack of deuterated species in the astrochemical network may influence these results, especially if the deuterated species, such as H_2D^+ and DCO^+ were to make a significant contribution to the charge budget. To examine this issue, we have considered the gas phase only deuteration modeling results of Hsu et al. (2021) with $f_D = 10$ and similar conditions as XR for P2. We find that deuteration only makes $\sim 20\%$ differences to the abundance of HCO^+ and so is not likely to be a major influence on our analysis.

Another caveat is the relative simplicity of the treatment of cosmic ray induced desorption. In particular, the modeling assumes a single value for the maximum temperature reached by the grains when they are hit by a cosmic ray. A more realistic treatment would allow for a distribution of such temperatures. In addition, variation of heating within an individual grain (e.g., Ivlev et al., 2015) is a feature that is also likely to be relevant and worthy of consideration in future analysis.

Finally, as discussed previously, there are a number of observational limitations. We have measured physical properties and chemical abundances averaged on scales of about 1 pc. In reality, these regions will contain a distribution of densities, temperatures, abundances, etc. In addition, a number of the regions considered are known to have sites of star formation, which will have very localised and strong variations in physical and chemical properties. While IRDCs do contain large amounts of relatively quiescent molecular gas and our study has included an effort to select regions that are free of known star formation, future studies making use of higher angular resolution data are warranted.

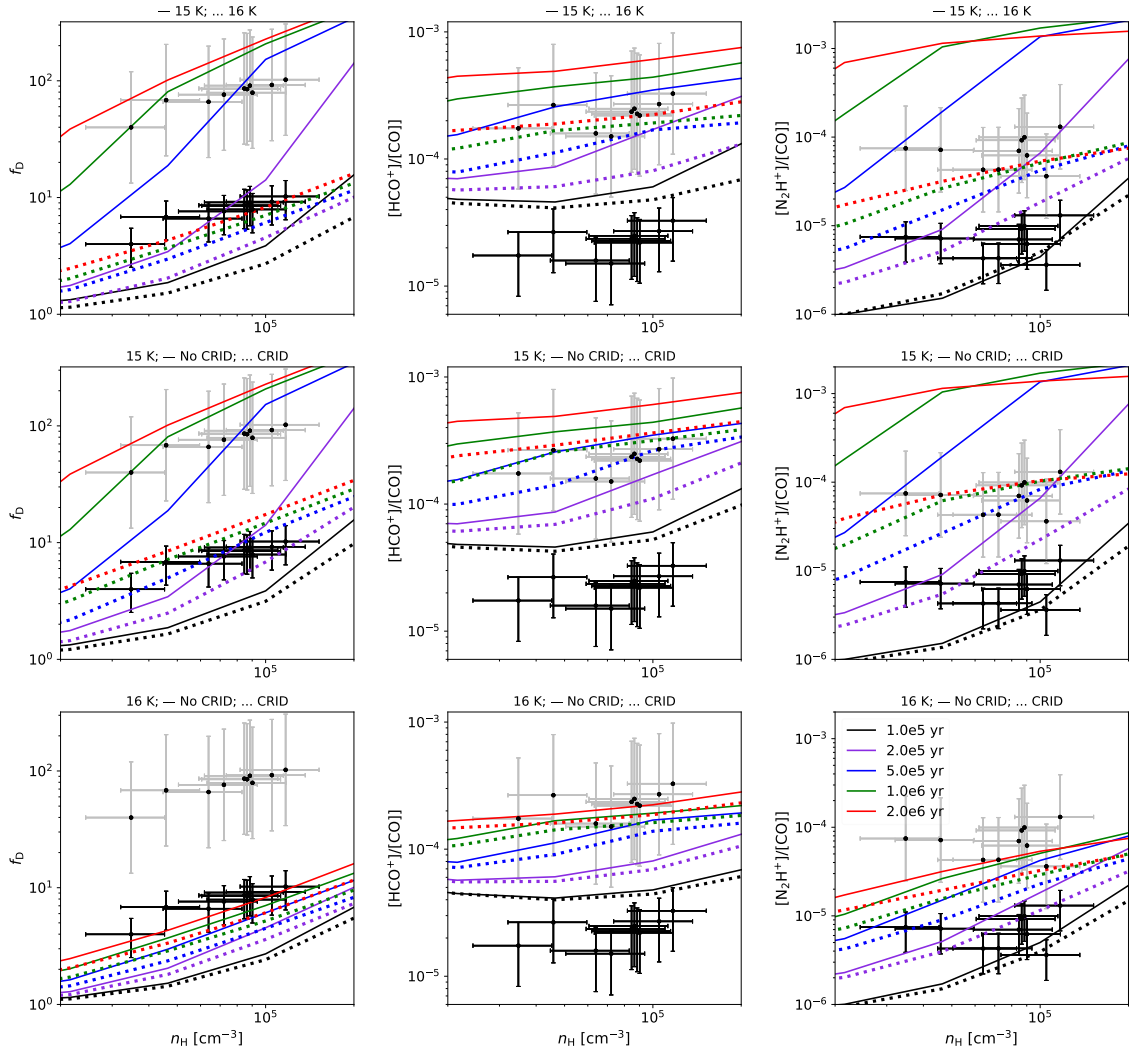

Figure 5.6: Exploration of Case 1 fitting of the whole IRDC clump sample, including trends with density. Left column panels show f_D versus $n_{\rm H}$; middle column panels show [HCO$^+$]/[CO] versus $n_{\rm H}$; right column panels show [N$_2$H$^+$]/[CO] versus $n_{\rm H}$. In all panels, the black points are the observed data, while grey points assume CO envelope contamination of 90% (see text). *(a) First row:* Temperature comparison; models have $\zeta = 2.2 \times 10^{-17}\,{\rm s}^{-1}$, $A_V = 20\,{\rm mag}$. Solid lines are from the models with $T = 15$ K and dotted lines from those of $T = 16$ K. *(b) Second row:* CRID comparison at 15 K; models have $\zeta = 2.2 \times 10^{-17}\,{\rm s}^{-1}$, $A_V = 20\,{\rm mag}$ and $T = 15$ K. Solid lines are from the models without Cosmic Ray Induced Desorption; dotted lines are with CRID. *(c) Third row:* CRID comparison at 16 K; results as (b), but with $T = 16$ K.

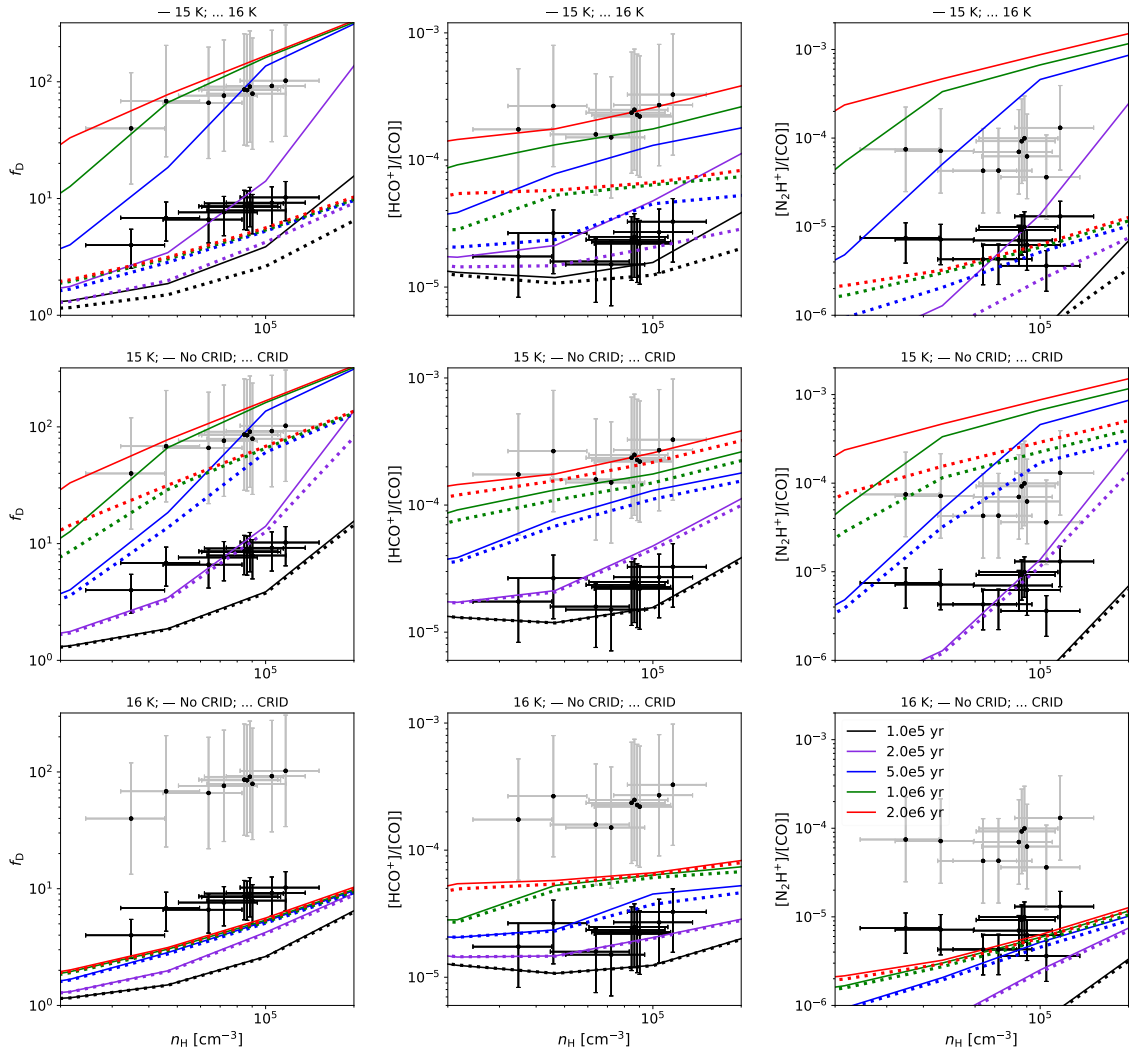

Figure 5.7: *(a) Top row; (b) middle row; (c) bottom row*: As Fig. 5.6, but with all models having $\zeta = 2.2 \times 10^{-18}$ s^{-1}.

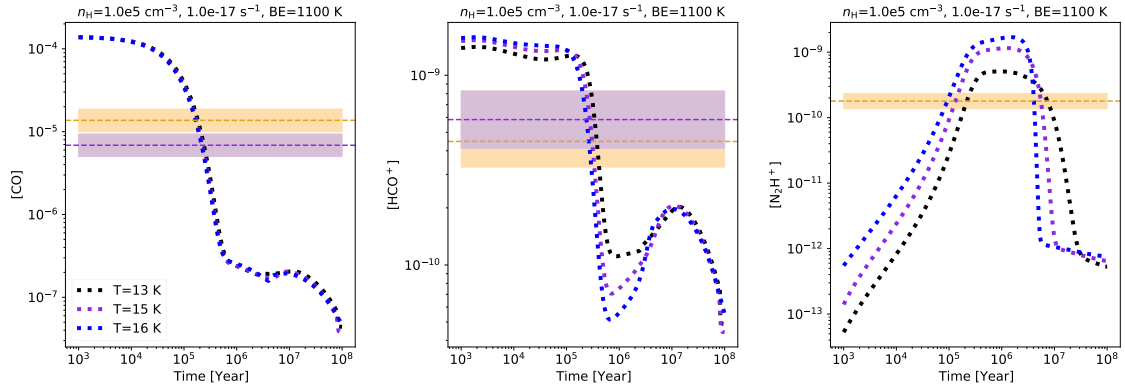

Figure 5.8: Evolution of [CO], [HCO^+] and [N_2H^+] in models with CO ice binding energy of 1100 K, $n_H = 1.0 \times 10^5$ cm^{-3}, $A_V = 20$ mag, $\zeta = 1.0 \times 10^{-17}$ s^{-1} and no CRID, exploring effects of different temperatures in the range relevant to IRDCs. The golden bands at each panel represent observed abundances at P2 ([HCO^+] from [$H^{13}CO^+$]) and the purple bands show [CO] reduced by a factor of 2 (allowing for potential CO envelope contamination) and [HCO^+] estimated from [$HC^{18}O^+$].

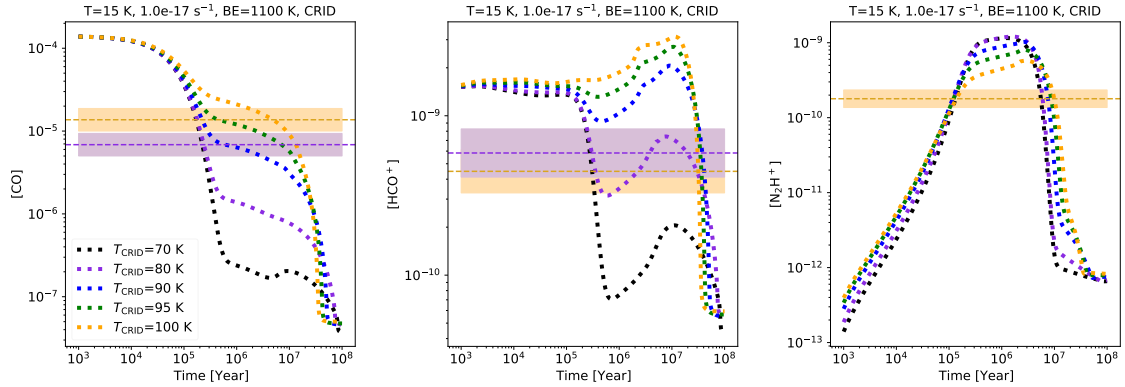

Figure 5.9: Evolution of [CO], [HCO^+] and [N_2H^+] in models with CO ice binding energy of 1100 K, $n_H = 1.0 \times 10^5$ cm^{-3}, $A_V = 20$ mag, $\zeta = 1.0 \times 10^{-17}$ s^{-1} and CRID, exploring values of T_{CRID} from 70 to 100 K. The golden bands in each panel represent observed abundances at P2 ([HCO^+] from [$H^{13}CO^+$]) and the purple bands show [CO] reduced by a factor of 2 (allowing for potential CO envelope contamination) and [HCO^+] estimated from [$HC^{18}O^+$].

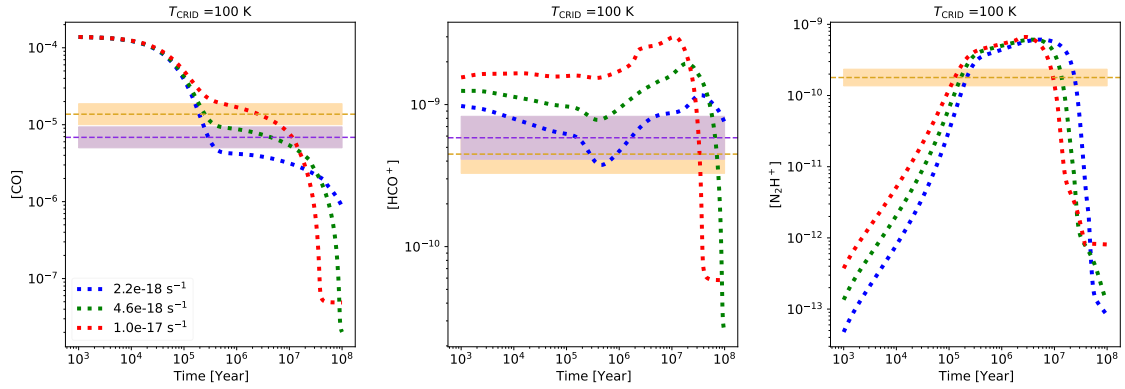

Figure 5.10: Evolution of [CO], [HCO^+] and [N_2H^+] in models with CO ice binding energy of 1100 K, $n_{\rm H} = 1.0 \times 10^5$ cm^{-3}, $A_V = 20$ mag, $T_{\rm CRID} = 100$ K and $\zeta = (0.22, 0.46, 1.0) \times 10^{-17}$ s^{-1}. The golden bands at each panel represent observed abundances at P2 ([HCO^+] from [$H^{13}CO^+$]) and the purple bands show [CO] reduced by a factor of 2 (allowing for potential CO envelope contamination) and [HCO^+] estimated from [$HC^{18}O^+$].

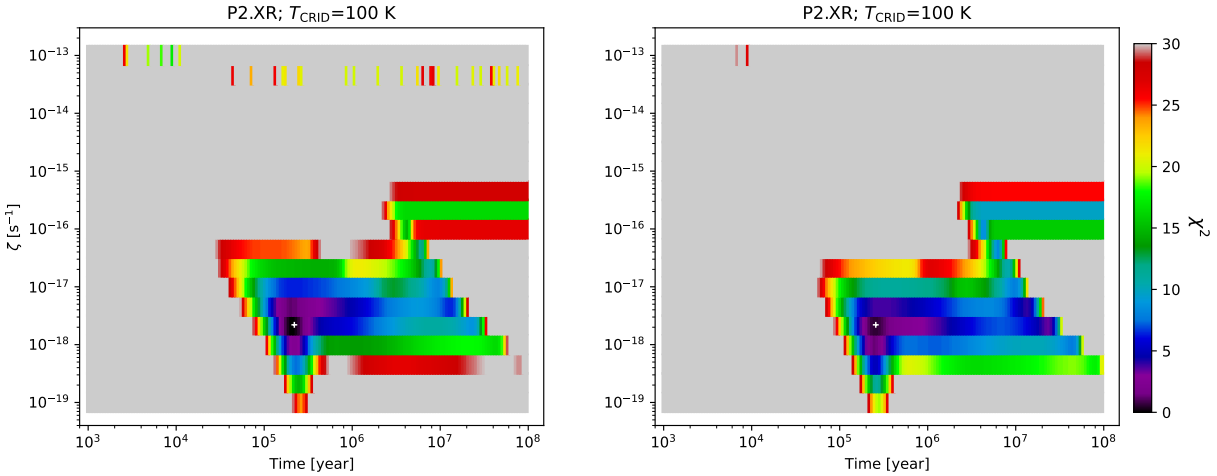

Figure 5.11: *(a) Left:* Example of XR Case 1 fitting of P2 abundances (HCO^+ from $HC^{18}O^+$) using astrochemical model Grid 2 (i.e., CO ice binding energy of 1100 K and $T_{\rm CRID} = 100$ K) showing the projected best χ^2 values in the ζ versus t plane. The location of minimum χ^2 is marked with a white cross. *(b) Right:* As (a), but now for [CO] reduced by a factor of two (allowing for potential CO envelope contamination).

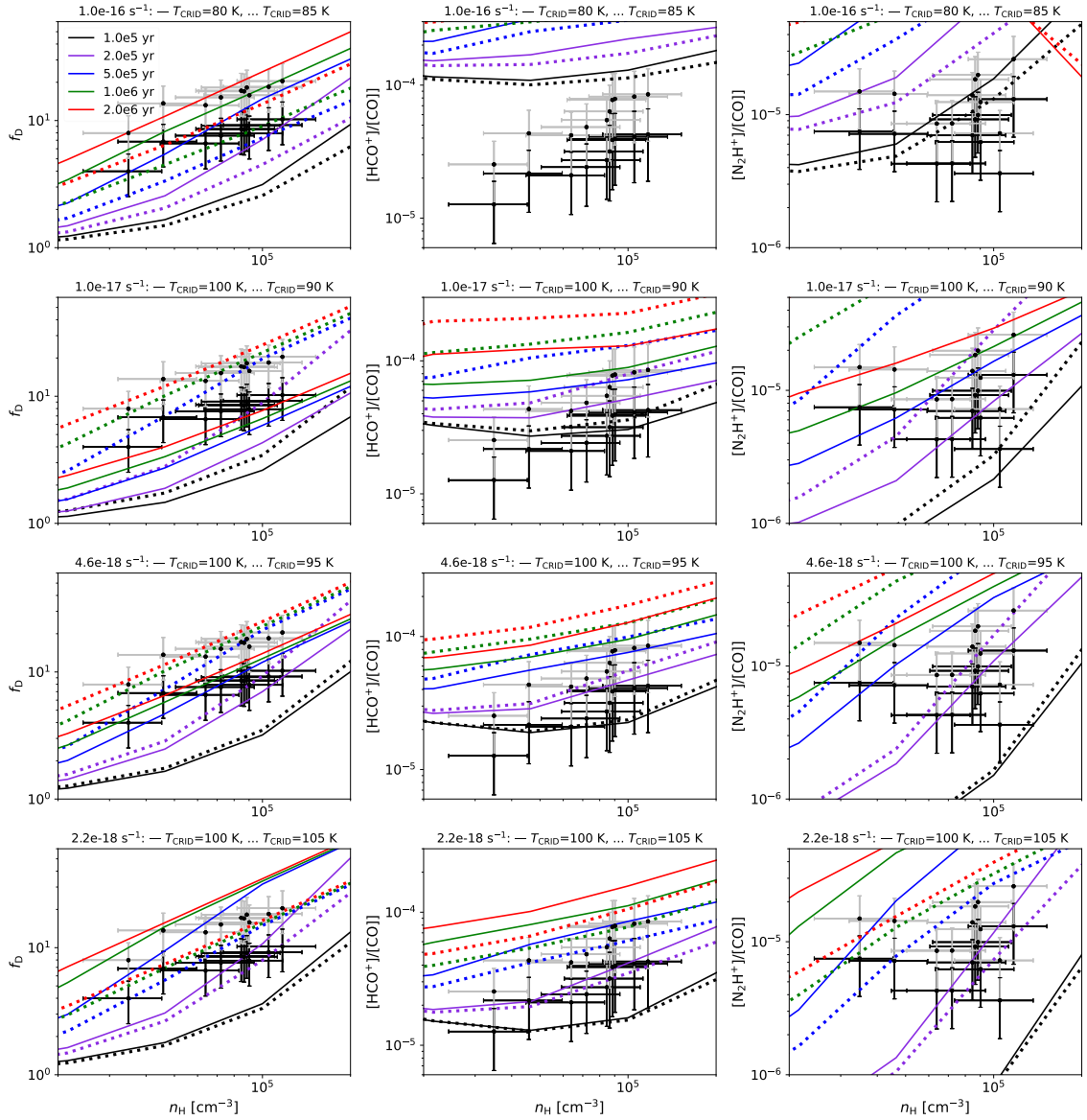

Figure 5.12: Exploration of Case 1 fitting of the whole IRDC clump sample, including trends with density, using models with gas temperature of $T = 15$ K, $A_V = 20$ mag, CO ice binding energy of 1100 K and exploring effects of cosmic ray induced desorption parameter $T_{\rm CRID}$. Left column panels show f_D versus $n_{\rm H}$; middle column panels show $[HCO^+]/[CO]$ versus $n_{\rm H}$; right column panels show $[N_2H^+]/[CO]$ versus $n_{\rm H}$. In all panels, black points are the actual observed data (with HCO^+ obtained from $HC^{18}O^+$), while the grey points assume CO abundance is reduced by a factor of 2 (due to CO envelope contamination). *(a) First row:* High CRIR case with $\zeta = 1.0 \times 10^{-16}\,{\rm s}^{-1}$. Solid lines are models with $T_{\rm CRID} = 80\,{\rm K}$ and dotted lines are those with $T_{\rm CRID} = 85\,{\rm K}$. As shown in the legend, the various colours correspond to models from 0.1 to 2 Myr. *(b) Second row:* Case with $\zeta = 1.0 \times 10^{-17}\,{\rm s}^{-1}$. Solid lines are models with $T_{\rm CRID} = 100\,{\rm K}$ and dotted lines are those with $T_{\rm CRID} = 90\,{\rm K}$. *(c) Third row:* Case with $\zeta = 4.6 \times 10^{-18}\,{\rm s}^{-1}$. Solid lines are models with $T_{\rm CRID} = 100\,{\rm K}$ and dotted lines are those with $T_{\rm CRID} = 95$ K. *(d) Fourth row:* Case with $\zeta = 2.2 \times 10^{-18}\,{\rm s}^{-1}$. Solid lines are models with $T_{\rm CRID} = 100$ K and dotted lines are those with $T_{\rm CRID} = 105$ K.

6
Conclusions

We have studied the astrochemical conditions in 10 positions in a massive IRDC. The abundances of eight species were measured via line emission observed from single dish IRAM-30m telescope observations, in combination with total mass surface density measurements from both *Herschel* dust emission and NIR+MIR extinction maps. The dust emission maps also enabled a measurement of temperature of the positions. To interpret these results an extensive grid of gas-grain astrochemical models was computed, exploring the effects of density, temperature, visual extinction of the Galactic FUV radiation field and cosmic ray ionization rate on the time evolution of the abundances of the observed species. Furthermore, additional parameters and features of the models, i.e., CO ice binding energy and effect of cosmic ray induced desorption, including an exploration of the transient heating temperature, were explored.

With various restrictions on the density, temperature and visual extinction, the standard astrochemical models (Grid 1) that best match CO, HCO^+ and N_2H^+ (Case 1) and all species (Case 2) have been found. For Case 1 fitting, these generally favor early time solutions (i.e., $t \sim 10^5$ yr), driven by CO freeze-out timescales, and with relatively low CRIRs. However, there are islands of low χ^2 at later times and higher CRIRs. Furthermore, Case 2 fitting can prefer these later times, although with worse values of χ^2.

We have discussed several aspects of the methodology that may be producing systematic errors, including the possibility of CO envelope contamination, high sensitivity to precise values of temperature near 15 K (or equivalently CO-ice binding energy assumptions) and cosmic ray induced desorption.

We have argued that the observed tightness of the CO depletion factor (f_D) versus density (n_H) relation argues against significant CO envelope contamination, since this would introduce significant scatter that is not observed. We have also proposed that the lack of scatter in the f_D-n_H relation does not favor solutions that rely on a fine tuning of temperature, but rather rely on the process of cosmic ray induced desorption to achieve a quasi-equilibrium later-time solution. Comparing to free-fall times, one would then favor models that show relatively tight, convergent behavior after a few $\times t_\mathrm{ff} \sim 0.3$ Myr. Such a conclusion would argue against rapid evolution of the IRDC structures on timescales that are as short as their local free-fall times. We have found that such models exist that well match the shape and normalisation of the f_D-n_H relation: e.g., models with $\zeta \sim 2$ to 4×10^{-18} s^{-1}, $T_\mathrm{CRID} \sim 100$ K, CO ice binding energy of 1100 K and ages of ~ 0.5 Myr (see Fig. 5.12c and d). Furthermore, these models also provide good matches to the observed $[HCO^+]/[CO]$ and $[N_2H^+]/[CO]$ versus n_H data. Within the framework of the presented models, we

are not able to find good solutions with cosmic ray ionization rates $\gtrsim$ few $\times 10^{-17}\mathrm{s}^{-1}$, since these overpredict the abundances of HCO^+ and N_2H^+. Such low rates of cosmic ray ionization are in contrast to measurements in the diffuse ISM (e.g., Neufeld and Wolfire, 2017), which may point to shielding of IRDC regions via their high column densities and/or magnetic field gradients.
Future work to extend this type of study to other IRDCs, including in different Galactic environments, and utilising higher angular resolution molecular line observations is desirable.

REFERENCES

Christopher J Barger and Robin T Garrod. Constraining cosmic-ray ionization rates and chemical timescales in massive hot cores. *The Astrophysical Journal*, 888(1): 38, 2020.

AT Barnes, S Kong, JC Tan, JD Henshaw, P Caselli, I Jiménez-Serra, and FRANCESCO Fontani. Widespread deuteration across the irdc g035. 39- 00.33. *Monthly Notices of the Royal Astronomical Society*, 458(2):1990–1998, 2016.

Shmuel Bialy. Cold clouds as cosmic-ray detectors. *Communications Physics*, 3(1): 1–7, 2020.

S. Bovino, S. Ferrada-Chamorro, A. Lupi, D. R. G. Schleicher, and P. Caselli. A new proxy to estimate the cosmic ray ionization rate in dense cores. , 495(1): L7–L11, March 2020. 10.1093/mnrasl/slaa048.

Emeric Bron, Evelyne Roueff, Maryvonne Gerin, Jérôme Pety, Pierre Gratier, Franck Le Petit, Viviana Guzman, Jan H Orkisz, Victor de Souza Magalhaes, Mathilde Gaudel, et al. Tracers of the ionization fraction in dense and translucent gas-i. automated exploitation of massive astrochemical model grids. *Astronomy & Astrophysics*, 645:A28, 2021.

Michael J Butler and Jonathan C Tan. Mid-infrared extinction mapping of infrared dark clouds: Probing the initial conditions for massive stars and star clusters. *The Astrophysical Journal*, 696(1):484, 2009.

Michael J Butler and Jonathan C Tan. Mid-infrared extinction mapping of infrared dark clouds. ii. the structure of massive starless cores and clumps. *The Astrophysical Journal*, 754(1):5, 2012.

Eric Carlson, Stefano Profumo, and Tim Linden. Cosmic-ray injection from star-forming regions. *Physical review letters*, 117(11):111101, 2016.

P. Caselli. Deuterated molecules as a probe of ionization fraction in dense interstellar clouds. , 50(12-13):1133–1144, October 2002. 10.1016/S0032-0633(02)00074-0.

P. Caselli, C. M. Walmsley, M. Tafalla, L. Dore, and P. C. Myers. CO Depletion in the Starless Cloud Core L1544. , 523(2):L165–L169, October 1999. 10.1086/312280.

P Caselli, CM Walmsley, M Tafalla, L Dore, and PC Myers. Co depletion in the starless cloud core l1544. *The Astrophysical Journal Letters*, 523(2):L165, 1999.

P Caselli, CM Walmsley, A Zucconi, M Tafalla, L Dore, and PC Myers. Molecular ions in l1544. ii. the ionization degree. *The Astrophysical Journal*, 565(1):344, 2002.

P. Caselli, F. F. S. van der Tak, C. Ceccarelli, and A. Bacmann. Abundant H_2D^+ in the pre-stellar core L1544. , 403:L37–L41, May 2003. 10.1051/0004-6361:20030526.

Paola Caselli, CM Walmsley, R Terzieva, and Eric Herbst. The ionization fraction in dense cloud cores. *The Astrophysical Journal*, 499(1):234, 1998.

C Ceccarelli, C Dominik, A López-Sepulcre, M Kama, M Padovani, E Caux, and P Caselli. Herschel finds evidence for stellar wind particles in a protostellar envelope: is this what happened to the young sun? *The Astrophysical Journal Letters*, 790(1):L1, 2014a.

Cecilia Ceccarelli, Paola Caselli, Dominique Bockelée-Morvan, Olivier Mousis, Sandra Pizzarello, Francois Robert, and Dmitry Semenov. Deuterium fractionation: the ariadne's thread from the pre-collapse phase to meteorites and comets today. *arXiv preprint arXiv:1403.7143*, 2014b.

Antonio Crapsi, Paola Caselli, Malcolm C Walmsley, and Mario Tafalla. Observing the gas temperature drop in the high-density nucleus of l 1544. *Astronomy & Astrophysics*, 470(1):221–230, 2007.

Richard M Crutcher. Magnetic fields in molecular clouds. *Annual Review of Astronomy and Astrophysics*, 50:29–63, 2012.

HM Cuppen, C Walsh, T Lamberts, D Semenov, RT Garrod, EM Penteado, and S Ioppolo. Grain surface models and data for astrochemistry. *Space Science Reviews*, 212(1-2):1–58, 2017.

C Favre, C Ceccarelli, A López-Sepulcre, FRANCESCO Fontani, R Neri, Sébastian Manigand, M Kama, P Caselli, A Jaber Al-Edhari, C Kahane, et al. Solis iv. hydrocarbons in the omc-2 fir4 region, a probe of energetic particle irradiation of the region. *The Astrophysical Journal*, 859(2):136, 2018.

F. Fontani, A. Giannetti, M. T. Beltrán, R. Dodson, M. Rioja, J. Brand, P. Caselli, and R. Cesaroni. High CO depletion in southern infrared dark clouds. , 423(3): 2342–2358, July 2012. 10.1111/j.1365-2966.2012.21043.x.

FRANCESCO Fontani, C Ceccarelli, C Favre, P Caselli, R Neri, Ian R Sims, C Kahane, FO Alves, N Balucani, E Bianchi, et al. Seeds of life in space (solis)-i. carbon-chain growth in the solar-type protocluster omc2-fir4. *Astronomy & Astrophysics*, 605:A57, 2017.

Brandt AL Gaches and Stella SR Offner. Exploration of cosmic-ray acceleration in protostellar accretion shocks and a model for ionization rates in embedded protoclusters. *The Astrophysical Journal*, 861(2):87, 2018.

C. Gieser, D. Semenov, H. Beuther, A. Ahmadi, J. C. Mottram, Th. Henning, M. Beltran, L. T. Maud, F. Bosco, S. Leurini, T. Peters, P. Klaassen, R. Kuiper, S. Feng, J. S. Urquhart, L. Moscadelli, T. Csengeri, S. Lumsden, J. M. Winters, S. Suri, Q. Zhang, R. Pudritz, A. Palau, K. M. Menten, R. Galvan-Madrid, F. Wyrowski, P. Schilke, Á. Sánchez-Monge, H. Linz, K. G. Johnston, I. Jiménez-Serra, S. Longmore, and T. Möller. Chemical complexity in high-mass star formation. An observational and modeling case study of the AFGL 2591 VLA 3 hot core. , 631:A142, November 2019. 10.1051/0004-6361/201935865.

Tatsuhiko I. Hasegawa and Eric Herbst. New gas-grain chemical models of quiscent dense interstellar clouds :the effects of H2 tunnelling reactions and cosmic ray induced desorption. , 261:83–102, March 1993. 10.1093/mnras/261.1.83.

Tatsuhiko I Hasegawa and Eric Herbst. New gas–grain chemical models of quiescent dense interstellar clouds: the effects of h2 tunnelling reactions and cosmic ray induced desorption. *Monthly Notices of the Royal Astronomical Society*, 261(1): 83–102, 1993.

Tatsuhiko I. Hasegawa, Eric Herbst, and Chun M. Leung. Models of Gas-Grain Chemistry in Dense Interstellar Clouds with Complex Organic Molecules. , 82: 167, September 1992. 10.1086/191713.

J. D. Henshaw, P. Caselli, F. Fontani, I. Jiménez-Serra, J. C. Tan, and A. K. Hernandez. Complex, quiescent kinematics in a highly filamentary infrared dark cloud. , 428(4):3425–3442, February 2013. 10.1093/mnras/sts282.

Jonathan D Henshaw, Paola Caselli, Francesco Fontani, Izaskun Jimenez-Serra, and Jonathan C Tan. The dynamical properties of dense filaments in the infrared dark cloud g035. 39- 00.33. *Monthly Notices of the Royal Astronomical Society*, 440(3): 2860–2881, 2014.

Audra K Hernandez and Jonathan C Tan. The dynamical state of filamentary infrared dark clouds. *The Astrophysical Journal*, 730(1):44, 2011.

Audra K. Hernandez, Jonathan C. Tan, Paola Caselli, Michael J. Butler, Izaskun Jiménez-Serra, Francesco Fontani, and Peter Barnes. Mapping Large-scale CO Depletion in a Filamentary Infrared Dark Cloud. , 738(1):11, September 2011. 10.1088/0004-637X/738/1/11.

Audra K Hernandez, Jonathan C Tan, Jouni Kainulainen, Paola Caselli, Michael J Butler, Izaskun Jiménez-Serra, and Francesco Fontani. A virialized filamentary infrared dark cloud. *The Astrophysical Journal Letters*, 756(1):L13, 2012.

Talayeh Hezareh, Martin Houde, Carolyn McCoey, Charlotte Vastel, and Ruisheng Peng. Simultaneous determination of the cosmic ray ionization rate and fractional ionization in dr 21 (oh). *The Astrophysical Journal*, 684(2):1221, 2008.

Chia-Jung Hsu, Jonathan C Tan, Matthew D Goodson, Paola Caselli, Bastian Körtgen, and Yu Cheng. Deuterium chemodynamics of massive pre-stellar cores. *Monthly Notices of the Royal Astronomical Society*, 502(1):1104–1127, 2021.

A. V. Ivlev, T. B. Röcker, A. Vasyunin, and P. Caselli. Impulsive Spot Heating and Thermal Explosion of Interstellar Grains Revisited. , 805(1):59, May 2015. 10.1088/0004-637X/805/1/59.

I Jiménez-Serra, P Caselli, F Fontani, JC Tan, JD Henshaw, J Kainulainen, and AK Hernandez. Gas kinematics and excitation in the filamentary irdc g035. 39-00.33. *Monthly Notices of the Royal Astronomical Society*, 439(2):1996–2013, 2014.

J. Kainulainen and J. C. Tan. High-dynamic-range extinction mapping of infrared dark clouds. Dependence of density variance with sonic Mach number in molecular clouds. , 549:A53, January 2013. 10.1051/0004-6361/201219526.

Robert C Kennicutt. The role of massive stars in astrophysics. *Proceedings of the International Astronomical Union*, 1(S227):3–11, 2005.

Shuo Kong, Paola Caselli, Jonathan C. Tan, Valentine Wakelam, and Olli Sipilä. The Deuterium Fractionation Timescale in Dense Cloud Cores: A Parameter Space Exploration. , 804(2):98, May 2015. 10.1088/0004-637X/804/2/98.

Shuo Kong, Jonathan C Tan, Paola Caselli, Francesco Fontani, Thushara Pillai, Michael J Butler, Yoshito Shimajiri, Fumitaka Nakamura, and Takeshi Sakai. The deuterium fraction in massive starless cores and dynamical implications. *The Astrophysical Journal*, 821(2):94, 2016.

Shuo Kong, Jonathan C. Tan, Paola Caselli, Francesco Fontani, Ke Wang, and Michael J. Butler. Zooming in to Massive Star Birth. , 867(2):94, November 2018. 10.3847/1538-4357/aae1b2.

Shuo Kong, Héctor G Arce, María José Maureira, Paola Caselli, Jonathan C Tan, and Francesco Fontani. Widespread molecular outflows in the infrared dark cloud g28. 37+ 0.07: Indications of orthogonal outflow-filament alignment. *The Astrophysical Journal*, 874(1):104, 2019.

R. Kuiper, H. Klahr, H. Beuther, and Th. Henning. On the stability of radiation-pressure-dominated cavities. , 537:A122, January 2012. 10.1051/0004-6361/201117808.

Richard B. Larson. Numerical calculations of the dynamics of collapsing proto-star. , 145:271, January 1969. 10.1093/mnras/145.3.271.

Francis LeBlanc. *An introduction to stellar astrophysics*. John Wiley & Sons, 2011.

Wanggi Lim, Jonathan C Tan, Jouni Kainulainen, Bo Ma, and Michael J Butler. The distribution of mass surface densities in a high-mass protocluster. *The Astrophysical Journal Letters*, 829(1):L19, 2016.

Dominique M Maffucci, Trey V Wenger, Romane Le Gal, and Eric Herbst. Astrochemical kinetic grid models of groups of observed molecular abundances: Taurus molecular cloud 1 (tmc-1). *The Astrophysical Journal*, 868(1):41, 2018.

D. McElroy, C. Walsh, A. J. Markwick, M. A. Cordiner, K. Smith, and T. J. Millar. The UMIST database for astrochemistry 2012. , 550:A36, February 2013. 10.1051/0004-6361/201220465.

Emily Moser, Mengyao Liu, Jonathan C Tan, Wanggi Lim, Yichen Zhang, and Juan Pablo Farias. The high-mass protostellar population of a massive infrared dark cloud. *The Astrophysical Journal*, 897(2):136, 2020.

Frédérique Motte, Sylvain Bontemps, and Fabien Louvet. High-Mass Star and Massive Cluster Formation in the Milky Way. , 56:41–82, September 2018. 10.1146/annurev-astro-091916-055235.

Frederique Motte, Sylvain Bontemps, and Fabien Louvet. High-mass star and massive cluster formation in the milky way. *Annual Review of Astronomy and Astrophysics*, 56:41–82, 2018.

David A Neufeld and Mark G Wolfire. The cosmic-ray ionization rate in the galactic disk, as determined from observations of molecular ions. *The Astrophysical Journal*, 845(2):163, 2017.

Karin I. Öberg, Guido W. Fuchs, Zainab Awad, Helen J. Fraser, Stephan Schlemmer, Ewine F. van Dishoeck, and Harold Linnartz. Photodesorption of CO Ice. , 662 (1):L23–L26, June 2007. 10.1086/519281.

KI Öberg, F Van Broekhuizen, HJ Fraser, SE Bisschop, EF Van Dishoeck, and S Schlemmer. Competition between co and n2 desorption from interstellar ices. *The Astrophysical Journal Letters*, 621(1):L33, 2005.

Marco Padovani, A Marcowith, P Hennebelle, and K Ferrière. Protostars: Forges of cosmic rays? *Astronomy & Astrophysics*, 590:A8, 2016.

Nicolas Peretto, GA Fuller, R Plume, LD Anderson, J Bally, C Battersby, MT Beltran, J-P Bernard, L Calzoletti, AM Digiorgio, et al. Mapping the column density and dust temperature structure of irdcs with herschel. *Astronomy & Astrophysics*, 518:L98, 2010.

T. Pillai, F. Wyrowski, S. J. Carey, and K. M. Menten. Ammonia in infrared dark clouds. , 450(2):569–583, May 2006. 10.1051/0004-6361:20054128.

A. Pon, D. Johnstone, P. Caselli, F. Fontani, A. Palau, M. J. Butler, M. Kaufman, I. Jiménez-Serra, and J. C. Tan. Mid-J CO shock tracing observations of infrared dark clouds. II. Low-J CO constraints on excitation, depletion, and kinematics. , 587:A96, March 2016. 10.1051/0004-6361/201527154.

J. M. Rathborne, J. M. Jackson, and R. Simon. Infrared Dark Clouds: Precursors to Star Clusters. , 641(1):389–405, April 2006. 10.1086/500423.

J. M. Rathborne, J. M. Jackson, E. T. Chambers, I. Stojimirovic, R. Simon, R. Shipman, and W. Frieswijk. The Early Stages of Star Formation in Infrared Dark Clouds: Characterizing the Core Dust Properties. , 715(1):310–322, May 2010. 10.1088/0004-637X/715/1/310.

J. M. Rathborne, G. Garay, J. M. Jackson, S. Longmore, Q. Zhang, and R. Simon. Hot Molecular Cores in Infrared Dark Clouds. , 741(2):120, November 2011. 10.1088/0004-637X/741/2/120.

Jill M Rathborne, JM Jackson, and R Simon. Infrared dark clouds: precursors to star clusters. *The Astrophysical Journal*, 641(1):389, 2006.

Jill M. Rathborne, James M. Jackson, Robert Simon, and Qizhou Zhang. Infrared dark clouds as precursors to star clusters. , 324(2-4):155–162, December 2009. 10.1007/s10509-009-0121-8.

Evelyne Roueff and Jacques Le Bourlot. Sustained oscillations in interstellar chemistry models. *Astronomy & Astrophysics*, 643:A121, 2020.

Frank H. Shu, Fred C. Adams, and Susana Lizano. Star formation in molecular clouds: observation and theory. , 25:23–81, January 1987. 10.1146/annurev.aa.25.090187.000323.

R Simon, JM Rathborne, RY Shah, JM Jackson, and ET Chambers. The characterization and galactic distribution of infrared dark clouds. *The Astrophysical Journal*, 653(2):1325, 2006.

Olli Sipilä, Kedron Silsbee, and Paola Caselli. A revised description of the cosmic ray-induced desorption of interstellar ices. *arXiv preprint arXiv:2106.04593*, 2021.

J. C. Tan, M. T. Beltrán, P. Caselli, F. Fontani, A. Fuente, M. R. Krumholz, C. F. McKee, and A. Stolte. Massive Star Formation. In Henrik Beuther, Ralf S. Klessen, Cornelis P. Dullemond, and Thomas Henning, editors, *Protostars and Planets VI*, page 149, January 2014. 10.2458/azu_uapress_9780816531240-ch007.

Jonathan Tan. Kinematics of a massive star cluster in formation. *hst*, page 13742, 2014.

Jonathan C. Tan, Shuo Kong, Michael J. Butler, Paola Caselli, and Francesco Fontani. The Dynamics of Massive Starless Cores with ALMA. , 779(2):96, December 2013. 10.1088/0004-637X/779/2/96.

Jonathan C. Tan, Shuo Kong, Yichen Zhang, Francesco Fontani, Paola Caselli, and Michael J. Butler. An Ordered Bipolar Outflow from a Massive Early-stage Core. , 821(1):L3, April 2016. 10.3847/2041-8205/821/1/L3.

Łukasz Tychoniec, Charles L. H. Hull, John J. Tobin, and Ewine F. van Dishoeck. Chemical and kinematic complexity of the very young star-forming region Serpens Main observed with ALMA. *IAU Symposium*, 332:249–253, September 2018. 10.1017/S174392131700967X.

F. F. S. van der Tak and E. F. van Dishoeck. Limits on the cosmic-ray ionization rate toward massive young stars. , 358:L79–L82, June 2000.

Floris F. S. van der Tak, Ewine F. van Dishoeck, II Evans, Neal J., and Geoffrey A. Blake. Structure and Evolution of the Envelopes of Deeply Embedded Massive Young Stars. , 537(1):283–303, July 2000. 10.1086/309011.

Catherine Walsh, TJ Millar, and Hideko Nomura. Chemical processes in protoplanetary disks. *The Astrophysical Journal*, 722(2):1607, 2010.

Catherine Walsh, Hideko Nomura, TJ Millar, and Yuri Aikawa. Chemical processes in protoplanetary disks. ii. on the importance of photochemistry and x-ray ionization. *The Astrophysical Journal*, 747(2):114, 2012.

Catherine Walsh, TJ Millar, and Hideko Nomura. Molecular line emission from a protoplanetary disk irradiated externally by a nearby massive star. *The Astrophysical Journal Letters*, 766(2):L23, 2013.

Catherine Walsh, Tom. J. Millar, Hideko Nomura, Eric Herbst, Susanna Widicus Weaver, Yuri Aikawa, Jacob C. Laas, and Anton I. Vasyunin. Complex organic molecules in protoplanetary disks. , 563:A33, March 2014. 10.1051/0004-6361/201322446.

Catherine Walsh, Hideko Nomura, and Ewine van Dishoeck. The molecular composition of the planet-forming regions of protoplanetary disks across the luminosity regime. , 582:A88, October 2015. 10.1051/0004-6361/201526751.

M. S. Westley, R. A. Baragiola, R. E. Johnson, and G. A. Baratta. Ultraviolet photodesorption from water ice. , 43(10):1311–1315, February 1995. 10.1016/0032-0633(95)00088-M.

Mark G Wolfire, David Hollenbach, and Christopher F McKee. The dark molecular gas. *The Astrophysical Journal*, 716(2):1191, 2010.

J. Woodall, M. Agúndez, A. J. Markwick-Kemper, and T. J. Millar. The UMIST database for astrochemistry 2006. , 466(3):1197–1204, May 2007. 10.1051/0004-6361:20064981.

S Zeng, Izaskun Jiménez-Serra, G Cosentino, S Viti, AT Barnes, JD Henshaw, P Caselli, F Fontani, and P Hily-Blant. 15n fractionation in infrared-dark cloud cores. *Astronomy & Astrophysics*, 603:A22, 2017.